ACS NANO

www.acsnano.org

ARTICLE

Three-Dimensional Encapsulation of *Saccharomyces cerevisiae* in Silicate Matrices Creates Distinct Metabolic States as Revealed by Gene Chip Analysis

Zeeshan Fazal,[†,‡,§] Jennifer Pelowitz,[∥] Patrick E. Johnson,[⊥,#] Jason C. Harper,[▽] C. Jeffrey Brinker,[*,∥,#] and Eric Jakobsson[*,¶,○,●,◇,◆]

[†]Beckman Institute for Advanced Science and Technology, [○]Carl R. Woese Institute for Genomic Biology, [‡]Department of Animal Sciences, [◆]Molecular and Integrative Physiology, [¶]Center for Biophysics and Computational Biology, [●]Neuroscience Program, and [◇]National Center for Supercomputing Applications, University of Illinois at Urbana-Champaign, Champaign, Illinois 61801, United States

[§]Department of Biosciences, COMSATS Institute of Information Technology, Park Road, Tarlai Kalan, Islamabad 45550, Pakistan

[∥]Advanced Materials Laboratory and [▽]Bioenergy and Biodefence Technologies, Sandia National Laboratories, Albuquerque, New Mexico 87185, United States

[⊥]Departments of Nanoscience and Microsystems Engineering, and [#]Chemical and Biological Engineering, Center for Engineered Materials, University of New Mexico, Albuquerque, New Mexico 87106, United States

Supporting Information

ABSTRACT: **In order to design hybrid cellular/synthetic devices such as sensors and vaccines, it is important to understand how the metabolic state of living cells changes upon physical confinement within three-dimensional (3D) matrices. We analyze the gene expression patterns of stationary phase *Saccharomyces cerevisiae* (*S. cerevisiae*) cells encapsulated within three distinct nanostructured silica matrices and relate those patterns to known naturally occurring metabolic states. Silica encapsulation methods employed were lipid-templated mesophase silica thin films formed by cell-directed assembly (CDA), lipid-templated mesophase silica particles formed by spray drying (SD), and glycerol-doped silica gel monoliths prepared from an aqueous silicate (AqS+g) precursor solution. It was found that the cells for all three-encapsulated methods enter quiescent states characteristic of response to stress, albeit to different degrees and with differences in detail. By the measure of enrichment of stress-related gene ontology categories, we find that the AqS+g encapsulation is more amenable to the cells than CDA and SD encapsulation. We hypothesize that this differential response in the AqS+g encapsulation is related to four properties of the encapsulating gel: (1) oxygen permeability, (2) relative softness of the material, (3) development of a protective sheath around individual cells (visible in TEM micrographs *vide infra*), and (4) the presence of glycerol in the gel, which has been previously noted to serve as a protectant for encapsulated cells and can serve as the sole carbon source for *S. cerevisiae* under aerobic conditions. This work represents a combination of experiment and analysis aimed at the design and development of 3D encapsulation procedures to induce, and perhaps control, well-defined physiological behaviors.**

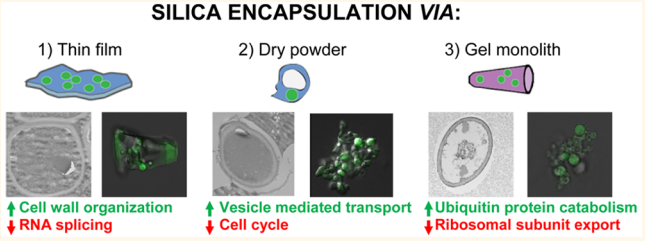

KEYWORDS: *living hybrid biomaterials, yeast stress response, yeast quiescent state, cell-directed assembly, glycerol modified silanes, sol–gel, spray drying*

Harnessing unique properties innate to biomolecules and living cells by incorporating them within hybrid materials continues to excite and inspire the efforts of researchers.[1−4] Such functional hybrid living materials may impact areas as diverse as biocatalysis, controlled delivery of therapeutics, stabilization of probiotics in food products, environmental and human health monitoring, industrial process monitoring, pollution remediation, early warning of warfare agents, advanced prosthetics, bioelectronics, and tissue/organ replacement.[5−12] Extensive techniques have been developed for

Received: September 21, 2016
Accepted: March 13, 2017
Published: March 13, 2017

DOI: 10.1021/acsnano.6b06385
ACS Nano 2017, 11, 3560−3575

incorporating biomolecules and living cells within materials that can maintain biological function, while providing stability outside the *in vivo* environment. For living cells, the majority of reported techniques rely on cellular encapsulation within polymeric materials that physically confine and protect the cells and can act as a synthetic extracellular matrix.[13,14] Successful matrices incorporate specific material properties that assuage chemical and mechanical stresses exerted on the integrated cells, provide access to oxygen, nutrients and molecules of interest, and allow for expulsion of metabolic wastes.[15−18] Many reports have implicated the importance of the interface chemistry between the cell surface and host matrix on meeting these requirements and enhancing long-term viability and activity.[19,20]

Encapsulation and physical confinement of living cells, however, can drastically alter the cellular environment and exert multiple stresses on the cells. Stresses commonly associated with encapsulation include compressive/tensile stress, osmotic stress, oxidative stress, acid/base exposure, nutrient depletion, temperature shock, and cytotoxic chemical exposure.[21−23] Unicellular organisms have evolved to rapidly respond to abrupt changes in environmental conditions by autonomous mechanisms that regulate gene expression profiles.[24] By altering the cell's metabolic state, cells can often maintain the vital functions and processes necessary for viability and growth.[25,26] As an example, some microorganisms encapsulate themselves in polymer matrix biofilms. These cells sense changes in their local environment (*e.g.*, quorum sensing) and alter their metabolic state, showing enhanced resistance to antibiotics, upregulation of virulence factors, development of competence, and changed growth morphology.[27]

As an alternative to organic polymers, amorphous silicon dioxide (SiO_2) and hybrid organosilicate matrices have also been used for cellular encapsulation. Generally, silica matrix encapsulated cells are physically confined such that growth and division is arrested. Metabolites and waste products must diffuse through the silica matrix, and the cell wall/membrane may interact with the polar and negatively charged silica surface, which is terminated with surface silanol ($\equiv$Si−OH) and deprotonated silanol ($\equiv$Si−O$^-$) groups. The metabolic state of living cells has been shown to change significantly upon physical confinement within silica matrices. For example, in response to this three-dimensional (3D) encapsulation, *Catharantus roseus* plant cells have been shown to substantially increase secondary metabolite (*i.e.*, alkaloid) production, demonstrating a 10−100-fold increase over cells free in solution.[28] This may be due to the cells shifting metabolic load from growth/division toward other metabolic pathways. Sol−gel immobilized *Escherichia coli* (*E. coli*) cells have also been reported to express GFP,[29] and produce ATP,[30] at levels nearly 2-fold greater than cells in solution. In these studies, the authors did not provide a hypothesis for this significant enhancement in biosynthesis. An individual *Staphylococcus aureus* (*S. aureus*) cell encapsulated in a nanostructured silica matrix was observed to self-initiate quorum sensing (QS) pathways due to constrained diffusion of quorum sensing "autoinducer" signaling molecules, showing that confinement alone can serve as a mechanism for inducing QS and its associated metabolic shifts.[31] Further, encapsulated QS *S. aureus* cells[31] and encapsulated QS *Serratia marcescens* (*S. marcescens*) cells[32] have significantly longer viability over encapsulated non-QS *S. aureus* and *S. marcescens*, indicating profound effects of encapsulation that have not as yet been well documented. The metabolic state of cells upon encapsulation can also significantly impact their ability to respond to the stresses of encapsulation. *Saccharomyces cerevisiae* (*S. cerevisiae*) cells from exponential phase culture (high metabolic activity) showed higher rates of induced gene expression than cells encapsulated from stationary phase cultures (low metabolic activity).[33] However, cells from stationary phase cultures exhibited significantly greater long-term viability. Further, addition of nutrients to the encapsulation matrix, which researchers expected to enhance long-term viability,[19] adversely impacted long-term viability. This was attributed to media components inducing exit of the cells from more robust metabolic states (*i.e.*, quiescence) and the metabolic production of toxic byproducts.

Despite significant efforts by many researchers to elucidate and characterize the condition of cells upon encapsulation, the physiological and metabolic state of these cells remains poorly understood. This is in part due to the challenges associated with probing cells within the encapsulation matrix and measuring the cellular response. Specifically, the "gold standard" measurement of viability is reproductive capability. As the vast majority of silica matrices physically restrict cells from growth and division[20] (with notable recent exceptions),[29,34] this technique for evaluating viability requires arduous procedures to free the cells from the matrix without compromising their integrity. Removal from the matrix may again alter the cellular state, or encapsulated cells may have entered an irreversible viable but nonculturable (VBNC) state,[35,36] such that they maintain metabolic activity but do not reproduce, making it challenging to draw conclusions from these measurements.[30]

To avoid these complications, it has become increasingly common for researchers to employ vital dye staining and fluorescence microscopy to report viability of encapsulated cells.[37] Vital dye staining typically assays cell membrane integrity and nonspecific enzyme activity; however, this technique has been shown to not always correlate with reproductive capability. Davey and Hexley reported that *S. cerevisiae* subjected to chemical and physical stresses stained with propidium iodide (PI), a membrane impermeant dye, indicative of cell death.[38] However, they also showed that some of the PI stained cells were able to recover and reproduce. Further, we recently reported that *E. coli* cells encapsulated in an aqueous silicate-based matrix showed compromised membrane integrity, but enhanced gene expression rates over cells in solution and retained reproductive capability when freed from the matrix.[39] This lack of correlation between membrane integrity, reproductive capacity, and protein expression highlights the complex relationship between the nanostructured inorganic matrix chemistry and the metabolic state of the encapsulated biological.

Herein, we present the genomic expression patterns of *S. cerevisiae* cells encapsulated within silica matrices and relate those patterns to known naturally occurring metabolic states. Gene ontology analysis of the genomic expression patterns comprehensively elucidates how systematic modifications of the encapsulating nanostructure influence cellular behavior. In this work, three distinct silica encapsulation methods were employed: lipid-templated mesophase silica thin films formed by cell-directed assembly (CDA),[40] lipid-templated mesophase silica particles formed by spray drying (SD),[36] and glycerol-doped silica gel monoliths prepared from an aqueous silicate (AqS+g) precursor solution.[33] *S. cerevisiae* cells from stationary phase cultures were used for encapsulation and as the reference condition for identifying differentially expressed genes. Gene enrichment analysis and grouping of biologically significant attributes *via* gene ontology (GO) revealed that distinct

DOI: 10.1021/acsnano.6b06385
ACS Nano 2017, 11, 3560−3575

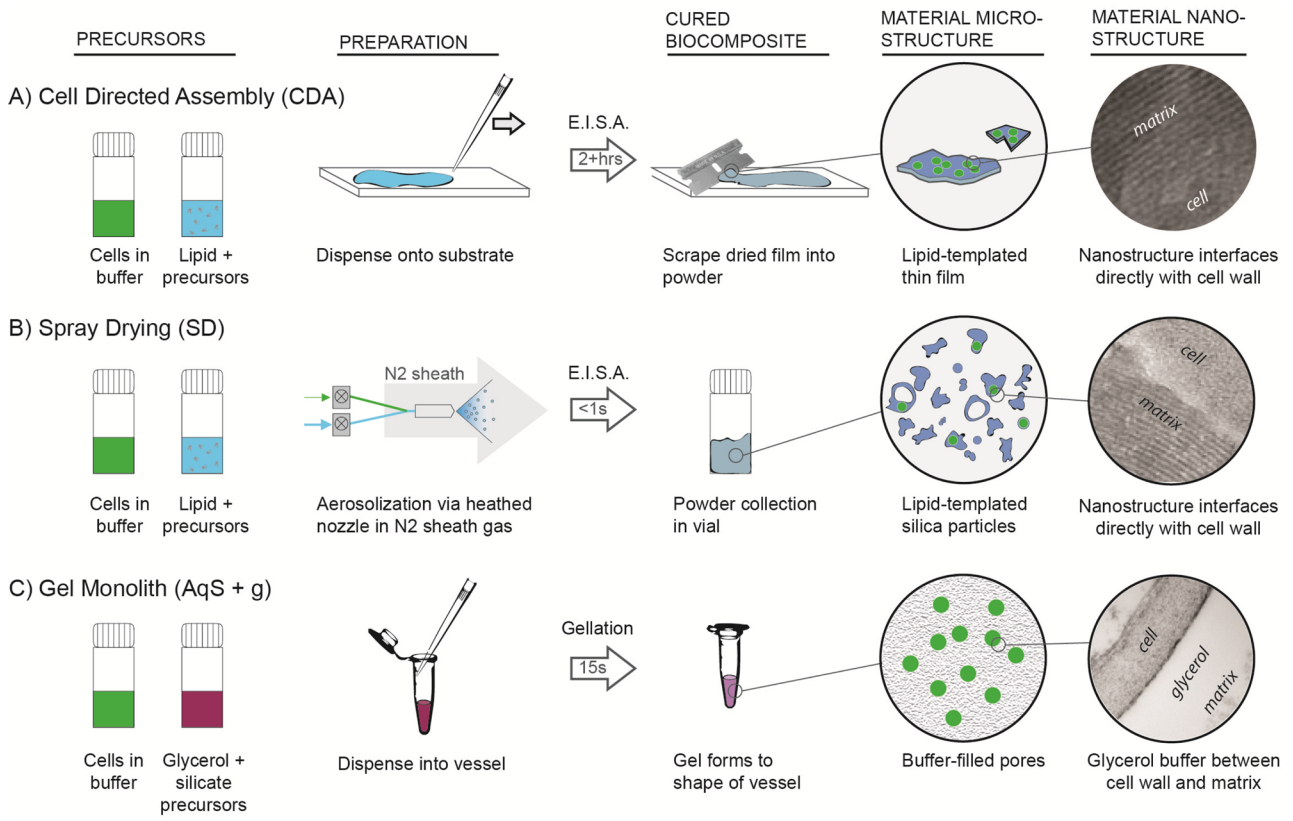

Figure 1. Schematic depicting the three cellular encapsulation methods investigated in this study. For all three methods, cells in buffer are mixed with precursor solution and either added to a substrate (A), spray dried (B), or added to a gelation vessel (C). In the first two cases, EISA drives the formation of a nanostructured lipid/silica encapsulating matrix, which results in a dry film (A) or powder (B), both of which exhibit a conformal ordered nanostructure as visualized by TEM. In the third case, gelation occurs within the sealed vessel, physically entrapping the cells within a highly porous matrix composed of aggregated silica nanoparticles that does not conform to the cell surface.

metabolic states were induced in *S. cerevisiae* from each encapsulation method. Further, the material properties at the bio−nano interface more profoundly influence biological behavior than the bulk chemistry of the matrix and the effect of physical confinement alone. Additionally, analysis of enriched gene data revealed the significant unique stresses exerted on cells from a particular encapsulation method and the cellular response to those stresses. This information will allow for informed tuning of encapsulation matrix parameters to improve upon desired biological traits and may facilitate the ability to induce, and perhaps control, new and unique physiological behaviors.

RESULTS AND DISCUSSION

We have examined the effects of three differing silica matrices with respect to the physiological and metabolic state of encapsulated *S. cerevisiae* cells and evaluated these effects with respect to the micro- to nanomorphologies of the material structure. The methods investigated include lipid-templated mesophase silica thin films formed by CDA, lipid-templated mesophase silica particles formed by SD, and glycerol-doped silica gel monoliths prepared from an aqueous silicate (AqS+g) precursor solution. The synthesis procedure used for each silica encapsulation method is shown schematically in Figure 1 and further detailed in the Materials and Method section.

In CDA (Figure 1A), short-chain phospholipids are used to direct the formation of an ordered lipid/silica mesophase during evaporation-induced self-assembly (EISA) of a silicate sol derived from acid-catalyzed hydrolysis of tetraethylorthosilicate (TEOS) in an ethanol/water solvent.[40]

When performed in the presence of living cells, the cells actively intervene to direct the formation of a novel bio−nano interface comprising a fluid, multilayered lipid/silica mesophase that interfaces coherently with the 3D silica nanostructure.[40] To prepare samples *via* CDA, cells in buffer and lipid dissolved in the silicate sol are prepared as described in the Materials and Methods section. These solutions are combined in a 1:1 ratio (v/v), mixed, and immediately applied to a cleaned glass slide. The solvent is allowed to evaporate (2+ h), yielding a thick glassy coating on the slide which can be scraped into a powder mechanically using a cleaned razor blade. The resulting powder is composed of large, flake-like particles that contain many cells packed together within a nanostructured lipid/silica matrix. TEM observations (Figure 1A, material nanostructure panel) reveal an ordered, conformal lipid/silica matrix that interfaces coherently with the cell surface. Here, two cells are shown with an intervening nanostructure exhibiting a striped pattern consistent with a cylindrical or lamellar lipid/silica mesophase as noted in previous work in which silica matrix formation is ordered by amphiphilic phospholipids.[40]

The SD method (Figure 1B) employs the same prehydrolyzed silica sol plus short-chain lipid solution as the CDA method, but ensures minimal contact between cells and somewhat cytotoxic precursor sol constituents (~15% ethanol v/v and pH 3) by mixing the cells and sol immediately prior to introduction to the spray nozzle. Cells and precursor solutions are prepared as with CDA samples, but they are combined *via* an automatic feed (peristaltic pumps) and aspirated into a heated, dry N_2 gas sheath forming small liquid droplets. Droplets dry very rapidly

DOI: 10.1021/acsnano.6b06385
ACS Nano 2017, 11, 3560−3575

(within ~400 ms), forming ordered lipid/silica mesophases in a manner related to aerosol-assisted EISA,[41] yielding solidified particles with size distributions from ~0.5 to 25 μm.[36] As with the CDA samples, TEM images (Figure 1B, material nanostructure panel) show a conformal striped nanostructure, consistent with a lamellar or hexagonal mesophase,[40] which again interfaces directly with the cell surface.

The third encapsulation matrix is a silicate gel monolith system, AqS+g (Figure 1C), which employs an aqueous sodium silicate precursor solution instead of the silicon alkoxide-based precursor solution as used in CDA and SD. The sodium silicate solution is hydrolyzed by ion exchange to create an acidified, aqueous silicic acid sol (pH 3), which, upon addition of cells in buffer, forms a porous silica gel monolith promoted by the accelerated rate of silica condensation at neutral pH.[42] Glycerol is added to the sol precursor solution prior to gelation and serves as an ameliorant against stresses exerted on the cells stemming from syneresis.[39] The precursor solution and cells in buffer (as before) are mixed briefly and immediately dispensed into a vessel (here, 1.5 mL microfuge tubes). The solution soldifies into a gel within ~15−30s and is further aged for 12−24 h to promote more complete silica condensation. The gel consists of a highly porous network of silica nanoparticles, which physically entraps cells plus buffer and glycerol. The silica nanoparticles are separated from the cell surface by a thin liquid layer, which may be enriched in glycerol (*vide infra*), as shown in the material nanostructure panel of Figure 1C.

Macro- and Nanomorphologies of Encapsulated Cells *via* Cell-Directed Assembly. While all *S. cerevisiae* cells in this study are encapsulated within a porous silica matrix, the physical properties at the bio−nano interface produced from each encapsulation method are markedly different. We have analyzed all three methods for their micro- and nanomorphologies using confocal fluorescence microscopy and transmission electron microscopy (TEM) and compared them with respect to their physical properties (Figures 2−4).

As depicted schematically in Figure 1 and observed by the eye, particles prepared using CDA appear rough and fragmented. Figure 2A−C shows the projection confocal (compressed z-stack) fluorescence and differential interference contrast (DIC) microscopy images of film fragments detailing the location of the encapsulated cells (fluorescently labeled green) within the lipid/silica fragments. Supplemental Figure S1 shows fluorescent line scans obtained as a function of z, where fluorescence quantification of the encapsulated cell *versus* autofluorescence of the lipid/silica matrix verifies 3D encapsulation of the cell within the matrix. Supplemental Figure S3 shows the corresponding individual slices of the complete z-stack shown in Figures 2−4.

Inspection of CDA samples with TEM reveals a tightly packed array of cells incorporated within a conformal nanostructured lipid/silica matrix that interfaces directly with the cell wall (Figure 2E, inset) as reported previously.[36,40] The "striped" nanostructure is consistent with an ordered lamellar or hexagonal lipid/silica mesophase as reported in previous work in which the formation of the silica matrix is directed by amphiphilic phospholipids.[40] Osmium tetroxide (OsO_4) staining of the cell wall allows for the visualization of the cells with respect to the lipid/silica matrix and emphasizes the conformal encapsulation of the cells. The ridge-like pattern observed in the TEM images is attributed to the high hardness (0.25 ± 0.10 GPa hardening to 0.52 ± 0.1 GPa with 15 day aging) and Young's modulus (4.3 ± 0.1 GPa, unchanging with 15 day aging) of the CDA

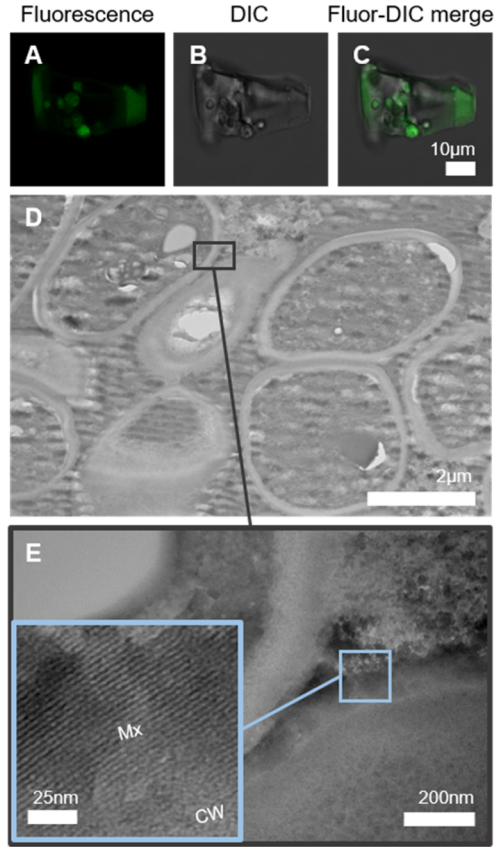

Figure 2. Micro- and nanomorphologies of CDA fragments show tightly packed cells. Fluorescence projection z-stack analysis verifies encapsulation, while TEM reveals an ordered nanostructured lipid/silica encapsulating matrix that interfaces with the cell surface. (A−C) Projection confocal fluorescence images of a small fragment highlight the placement of cells within the particle. (The green bands at the edge of the particle are an optical artifact resulting from refraction of the green fluorescence occurring within the glass-like particle). (D) TEM analysis shows a very dense cell loading within the particle and a zoomed image (E) reveals an ordered nanostructured matrix that, here, is highlighted between two cells. The inset clearly shows an ordered nanostructure interfacing between two cell walls. CW: cell wall; Mx: matrix.

samples, which exceed those of many natural and synthetic composites and cause "chattering" of the ultramicrotome blade as described previously.[36] This phenomenon is also evident with the SD samples, but not with the relatively soft gel materials (*vide infra*).

Macro- and Nanomorphologies of Encapsulated Cells *via* Spray Drying. Here, using the same precursor chemistry as with CDA, we have extended our scalable, SD process as developed previously for *E. coli*[36] to spray dried lipid/silica particles containing eukaryotic organisms (Figure 3). As shown schematically in Figure 1, compared to CDA, SD involves extremely short cell-solvent contact times due to the mixing chamber and very short residence/drying times of ~400 ms.[43] Furthermore, this technique allows for the facile preparation of large quantities of biomaterial with tight control over material macromorphologies (size, shape, approximate cell loading), while independently maintaining the material properties (specifically nanostructure and hardness).

As observed using confocal fluorescence microscopy (Figure 3A−C), SD particles appear as aggregates of smaller particles. Shown is an optical slice within the z-stack of the particle

DOI: 10.1021/acsnano.6b06385
ACS Nano 2017, 11, 3560−3575

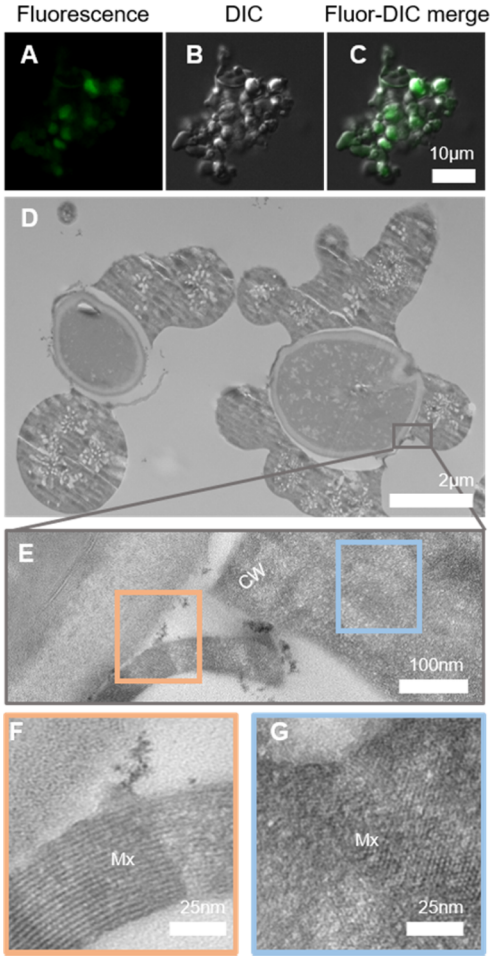

Figure 3. Micro- and nanomorphologies of SD particles reveal distribution of cells within dry, spray-dried powders. (A–C) Projection confocal fluorescence image (A), DIC image (B), and merged image (C) of a particle fragment highlight the placement of cells within the particle. The z-stack gallery and compressed z-stack image (Supplemental Figure S3B) show about 6 embedded cells. (D) TEM analysis shows cells encapsulated within a conformal, ordered lipid/silica matrix in addition to whole lipid/silica particles, which contain no cells as described previously.[36] The chattering in the ultramicrotomed section is attributed to the high hardness and Young's modulus of the silica nanostructure as described previously.[36] (E) A zoomed image shows the interface of the lipid/silica nanostructure and the cell which appears to be "peeling off" from the cell surface. The nanostructure is clearly visible and interfaces directly with the cell surface (F) and extends into the bulk of the particle (G). CW: cell wall; Mx: matrix. Both the peeling and separation of the matrix from the cell are attributed to sample preparation artifacts given correspondence of the shape of the separated matrix and cell surface.

depicting the placement of several cells within the center of the particle. The full z-stack gallery including the z-stack merge image can be found in Supplemental Figure S3.

TEM images of SD samples highlight the differing microstructure found with this class of material, which comprises individual or multiple cells incorporated within distinct, isolated macroscopic particles that preserve the conformal ordered lipid/silica nanostructure observed for CDA samples. Figure 3D highlights two *S. cerevisiae* cells encapsulated within two larger particles, showing a distinct layer of matrix "peeling" off from the surface of the cell—an artifact produced during sample preparation *via* solvent exchange or microtoming. This thin shell surrounding the cell is a further indication that the cell is completely encapsulated within the silica matrix. Figure 3E magnifies the interface between the cell and the matrix, and zoomed insets clearly show an ordered lamellar structure (Figure 3F) immediately adjacent to the cell wall with a lamellar/hexagonal mesophase (Figure 3G) extending throughout the bulk of the particle. These data suggest that the encapsulation of *S. cerevisiae* cells within this class of spray dried nanostructured lipid/silica matrix exhibits essentially identical nanoproperties to those observed for bacteria encapsulated in the same spray-drying procedure and exhibits a similar-sized nanostructure with ~3 nm lamellar features (Figure 3F).[36] Similar to CDA specimens, these TEM images show a distinct chattering pattern in the material microstructure, which we attribute to the high hardness (1.4 ± 0.1 GPa) and elastic modulus (13.0 ± 0.1 GPa) of the encapsulating lipid/silica mesophase. It is worth noting that, based on our previous study with *E. coli*, the reported hardness and Young's modulus of SD samples as compared to CDA samples are ~3–6 times and ~3 times higher, respectively, and the TEM images presented herein reflect a more distinct fatigue pattern with the SD samples as compared to the CDA samples. For comparison, TEM images of gel samples (Figure 4D) exhibit no discernible chattering pattern (*vide infra*).

Macro- and Nanomorphologies of Encapsulated Cells *via* Aqueous Gel Monoliths. Encapsulation of cells within silica gels has been extensively studied,[17] where cells are introduced into an aqueous silica sol and are physically entrapped by pH-triggered, base-catalyzed silica condensation[44] with no accompanying drying and little to no shrinkage. Figure 4A–C

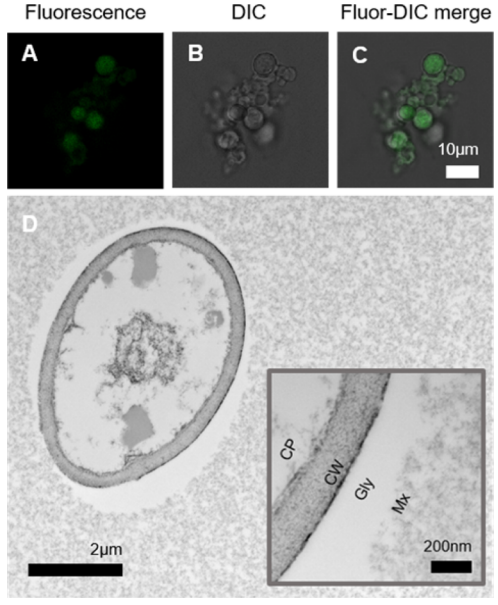

Figure 4. Micro- and nanomorphologies of gel particles show cells that are individually incorporated within an amorphous matrix and are surrounded by a glycerol sheath. (A–C) Projection confocal fluorescence images of a small particle highlight the placement of cells within the particle. The z-stack gallery and compressed z-stack image (Supplemental Figure S3C) show cell placement within a gel particle. (D) TEM images of an individual cell show incorporation within a ramified, highly porous matrix composed of small (10 nm) primary silica nanoparticles that is separated from the cell surface by a 20–450 nm thick porous layer that is rich in glycerol. CP: cytoplasm; CW: cell wall; Gly: glycerol; Mx: matrix.

DOI: 10.1021/acsnano.6b06385
ACS Nano 2017, 11, 3560–3575

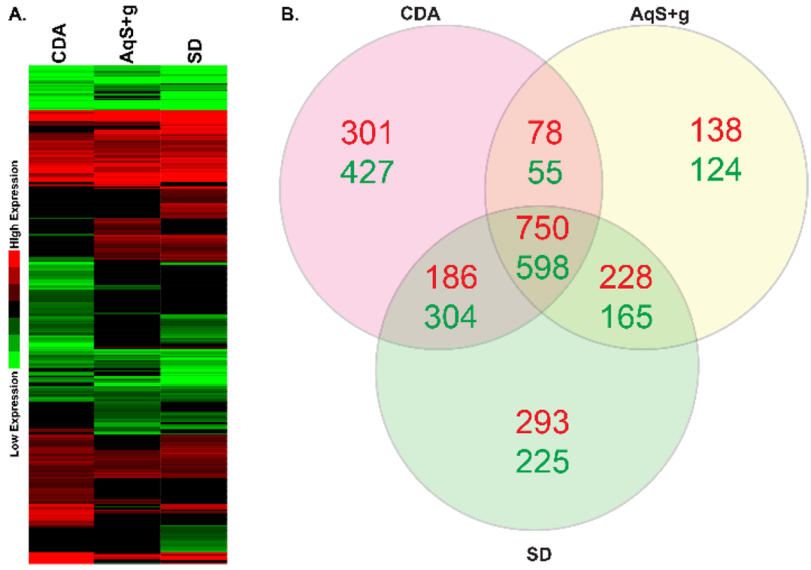

Figure 5. (A) Hierarchical clustering with Euclidean distance and complete linkage of differentially expressed genes at a B&H corrected *p*-value <0.05 and log 2-fold change of >1 and <-1 for upregulated and downregulated genes, respectively, providing an overview of gene expression profiles in each encapsulated method. (B) Distribution of all differentially expressed genes from *S. cerevisiae* cells encapsulated within three differing silica matrices: CDA, SD, and AqS+g. Upregulated genes are shown in red. Downregulated genes are shown in green.

shows confocal fluorescence and DIC images of a gel fragment, where a random incorporation of cells within a nonfluorescent silica gel fragment is observed. A z-stack gallery and a compressed z-stack image (Supplemental Figure S3C) verify the random placement of the cells within the gel particle. Figure 4D shows a TEM image of an individual cell entrapped within the silica gel matrix. Because the gel maintains the same relative volumes of the constituent components as the sol, and no evaporation occurs (as opposed to the CDA and SD samples), the cells appear individually isolated within the gel matrix (Figure 4D). This matrix is comprised of a highly porous, ramified network of aggregated 10 nm silica nanoparticles, as expected from extensive previous experiments confirming the fractal nature of amorphous silica gels.[20,45,46] Importantly, Figure 4D and the magnified inset distinctly emphasize that, compared to CDA or SD, the silica gel matrix does not conform to the cell surface and is separated by a boundary region which is rich in glycerol. Also, noteworthy as mentioned above, the gel sample is notably less hard/stiff than the CDA and SD samples and does not exhibit any chattering during microtoming.

RNA Expression Levels of Encapsulated *S. cerevisiae* Cells. To more comprehensively explore the physiological and metabolic state induced by each silica encapsulation matrix, genetic analysis was performed using *S. cerevisiae* cells from stationary phase cultures (7 day old cultures). Cells in this state are more resistant to a multitude of stresses and have shown greater long-term viability when integrated within hybrid abiotic materials.[31−33] *S. cerevisiae* cells in stationary phase cultures have undergone two metabolic shifts. In the first shift, rapidly proliferating cells in exponential culture deplete all fermentable carbon and undergo slow carbon starvation. The cells alter their metabolism (diauxic shift) to consume ethanol and nonfermentable carbon byproducts of fermentation. After all fermentation byproduct carbon is depleted, the cells again shift their metabolism, with a portion of the cells entering quiescence, a maintenance-like resting state where proliferation does not occur and cells can remain viable without nutrients.[47] Cells from the stationary phase were used in all three silica encapsulation matrices and were also used as the baseline condition to which encapsulated cell RNA expression levels were referenced. Identification of differentially expressed genes, and identification of GO,[48] followed the method of Benjamini and Hochberg[49] by the Database for Annotation, Visualization, and Integrated Discovery (DAVID),[50] as described in the Materials and Methods section.

An overview of gene expression profiles of cells encapsulated by each of three encapsulated methods is presented in a heat map format in Figure 5A. The extent to which the three-encapsulation methods used in this work induce similar genetic expression patterns, and the extent to which they differ, is also summarized in Venn Diagram form in Figure 5B. Generally, all three methods share 750 and 598 upregulated and downregulated genes, respectively. However, CDA has 427 downregulated and 301 upregulated alone, followed by SD (225 downregulated, 293 upregulated) alone. The AqS+g method has the least unique number of genes differentially downregulated (138) and upregulated (124).

Gene Ontology Analysis of RNA Expression. Genes for whom the biological function is known can be categorized into three GO domains: biological process (BP), molecular function (MF), and cellular component (CC). BP terms refer to genes associated with multistep events requiring organized assembly of molecular functions (*e.g.*, RNA transport, autophagy, biosynthesis). MF terms describe genes that participate in single-step elemental activities at the molecular level, such as binding or catalysis. ATP-binding, hydrolase activity, and toll receptor binding are examples of MF terms. Genes associated with components of cells, or the extracellular environment, are described as CC terms. Example of CC terms include protein dimers, ribosomes, mitochondrion, and cell wall.

The distribution of enriched GO terms for upregulated and downregulated genes from *S. cerevisiae* cells encapsulated within each silica matrix is presented in Figure 6. In the BP domain (Figure 6), many GO terms are shared between all three methods for both up and down regulated genes. The CDA method showed more upregulated enriched GO terms (14) than the

DOI: 10.1021/acsnano.6b06385
ACS Nano 2017, 11, 3560−3575

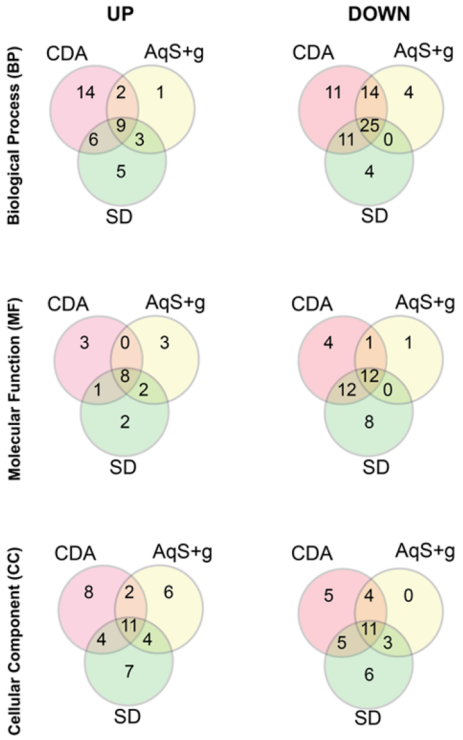

Figure 6. GO categorization of differentially expressed genes from silica matrix encapsulated *S. cerevisiae* cells. GO domains: BP, MF, and CC. Silica encapsulation matrices: CDA, SD, and AqS+g.

other encapsulation methods (SD: 5; AqS+g: 1), with 9 shared GO terms between all three methods. For the downregulated genes, 25 GO terms are shared between three methods, however, the CDA method showed significantly more enriched BP terms (11) than the other two methods (SD: 4; AqS+g: 4). A significant majority of downregulated BP terms (14) are shared between the CDA and AqS+g methods. Also, cells encapsulated *via* CDA and SD shared 11 downregulated BP terms. In aggregate, these data show that all three methods shared more BP terms than were unique to any one method of encapsulation. However, each of the encapsulation procedures produced some uniquely enriched classes.

In the MF GO domain (Figure 6), the majority of upregulated (8) and downregulated (12) terms are again shared between all three methods. Downregulated MF terms show little difference between the encapsulation methods with respect to number of unique MF terms (CDA: 4; SD: 8; AqS+g: 1). These data indicate that AqS+g encapsulated *S. cerevisiae* cells in particular show a similar MF associated gene expression compared to cells in a stationary state.

In the CC GO domain (Figure 6), the largest number of upregulated (11) and downregulated (11) CC GO enriched classes are shared by all three methods, followed by upregulated CC terms unique to CDA (8) and SD (7). Cells encapsulated in SD and CDA methods have a greater number of unique downregulated CC terms (6 and 5, respectively) than AqS+g, which has none.

Identification of Differentially Enriched GO Terms. Groupings of GO enrichment terms for BP for encapsulated *S. cerevisiae* are presented in scatter plots by REVIGO[51] comprising Figures 7, 9, and 10. The scatter plots show the represented functional clusters after removing redundant terms by REVIGO.[51] The GO terms that are semantically similar should position together in the scatter plot and semantic space (*X*, *Y*), but it should be noted that the *X*,*Y* coordinate units have no inherent meaning. The size of the circle is relative to the frequency of the GO term in the underlying GO database; the color of the circle represents the log 10 *p*-value. The threshold used for allowed sematic similarity is "medium." The corresponding complete listings of GO enrichment terms are provided in Supporting Information File 2, as are associated B&H corrected *p*-values for the GO enrichments.

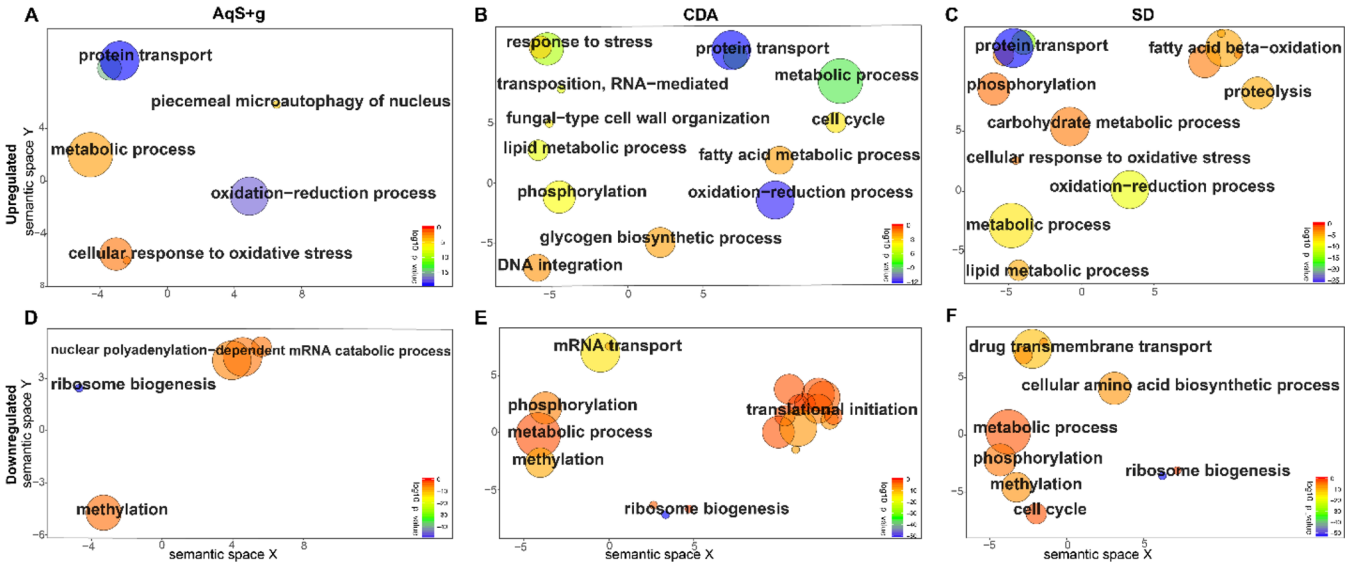

Figure 7. GO enrichment of BP terms as determined according to the DAVID. Redundant GO terms were removed and then summarized by REVIGO and represented as scatter plot. (A−C) Upregulated biological processes for *S. cerevisiae* encapsulated *via* (A) AqS+g, (B) CDA, and (C) SD. (D−F) Downregulated biological processes for *S. cerevisiae* encapsulated *via* (D) AqS+g, (E) CDA, and (F) SD. GO terms are shown by circles and plotted by semantic similarity with other GO terms; circles closer to each other shows closely related GO terms. The size of the circle is relative to the frequency of the GO term in the underlying GO database. Circle color represents the log 10 *p*-value. GO terms with B&H corrected *p*-value <0.05 are shown.

DOI: 10.1021/acsnano.6b06385
ACS Nano 2017, 11, 3560−3575

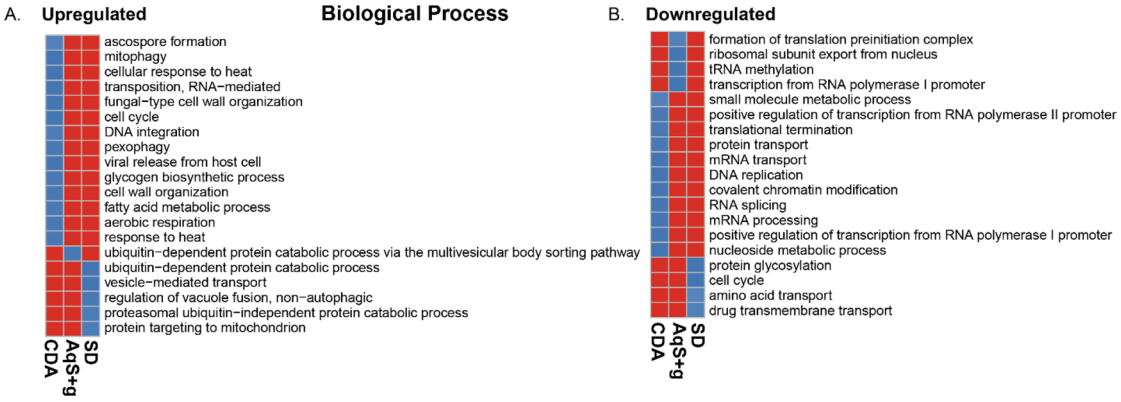

Figure 8. BP GO terms that are uniquely enriched in each of the three encapsulation methods. GO enrichment was determined *via* the DAVID. (A) Upregulated and (B) downregulated BP for *S. cerevisiae* encapsulated *via* AqS+g, CDA, and SD. Red colored boxes show an absence of a GO term, while blue colored boxes show a presence of a GO term in the given encapsulation method. GO terms with B&H corrected *p*-values <0.05 are shown. Individual B&H corrected *p*-values are shown in Supporting Information File 2.

In the following discussion, it is important to keep in mind that up- or down-regulation of expression of genes associated with a BP may not be synonymous with up- or down-regulation of the process itself. Some of the genes may activate the process in question, while others may inhibit it. Depending on overall feedback mechanisms, genes associated with activating a process may be upregulated to exploit availability of a substrate, while in other cases, they may be upregulated to compensate for scarcity of a substrate. The only completely reliable inference to draw from enrichment of a gene ontology is with respect to association in some way with the process in question.

Enrichment of BP GO terms in each of encapsulation method is shown in Figure 7. All three methods show upregulated enrichment in cellular response to oxidative stress, proteolysis, oxidation−reduction process, protein transport, and piecemeal microautophagy of nucleus (Figure 7A). Proteolysis is one of the key responses to stress as damaged proteins need to be eliminated from the cell.[24] Furthermore, reactive oxygen species (ROS) generated through oxidative phosphorylation can lead to chemical reactions that damage cells, which leads in turn to activation of oxidative stress responses from the cell.[24] All of these processes are generally implicated in the stress response.[24] Lipid and carbohydrate metabolic processes are upregulated in both SD and CDA (Figure 7B,C and Supporting Information File 2 respectively). CDA and SD (but not AqS+g) share the upregulated BP term phosphorylation. Cells encapsulated *via* CDA showed upregulated cell wall organization terms (Figure 7B) as a response to weakened cell walls during stress. SD-encapsulated cells showed upregulated responses associated with obtaining energy by fatty acid beta oxidation (Figure 7C).

All three methods show downregulated enrichment in ribosome biogenesis, methylation, amino acid biosynthetic process, and a cluster of terms related to RNA processing (Figure 7D−F, Supporting Information File 2). Ribosome biogenesis and processing of RNAs such as tRNA or rRNA use a significant amount of energy, and cells need to lower the expression of these genes to conserve energy under unfavorable conditions.[24] Reduction in expression level of ribosome biogenesis and RNA processing can be interpreted as a reduction in cell growth.[52] Furthermore, the expression of genes associated with translation and tRNA aminoacylation is reduced as a general response to stress (Supporting Information File 2). Downregulation of these processes is a characteristic feature of stress response.[24] Terms shared between CDA and SD, but not AqS+g, include metabolic process and phosphorylation. Both terms were also enriched in upregulated genes from CDA and SD, indicating cells from both methods have significantly changed their metabolic states and phosphorylation profiles in response to stress (Figure 7B,C,E,F).

BP GO terms that are unique to each of the three encapsulation methods (as mentioned in Figure 6) show that the different methods of encapsulation have some distinctly different effects on gene expression patterns (Figure 8). Upregulated genes in CDA are uniquely enriched in ascospore formation, fungal-type cell wall organization, aerobic respiration, glycogen biosynthetic process, and response to heat (Figure 8A). Ascospore formation in yeast is implicated in response to nutrition deprivation that allows cells to produce stress-resistant haploid spores.[53] Furthermore, upregulated CDA genes are enriched in mitophagy and pexophagy (Figure 8A). Both mitophagy and pexophagy are selective autophagy processes to remove damaged mitochondria and peroxisomes, respectively, in response to stress.[54,55] Upregulated genes in SD are uniquely enriched in protein targeting to mitochondrion, vesicle-mediated transport, regulation of vacuole fusion, and BP GO terms related to protein catabolism (Figure 8A). Upregulated genes in AqS+g are only enriched in the ubiquitin-dependent protein catabolic process *via* the multivesicular body sorting pathway (Figure 8A). Upregulation of ubiquitin dependent protein degradation is implicated in stress, as damaged proteins are degraded by ubiquitination to adjust the cellular protein repertoire to cope with the new environment.[24]

Differentially downregulated genes in CDA are uniquely enriched in covalent chromatin remodeling, RNA splicing, protein transport, mRNA transport, mRNA processing, DNA replication, nucleoside metabolism, and small metabolic processes, consistent with the observation that these processes are energy consuming and their expression levels are reduced under stress (Figure 8B).[24] Differentially downregulated genes in AqS+g are uniquely enriched in tRNA methylation, formation of translation preinitiation complex, transcription from RNA polymerase I promoter, and ribosomal subunit export from nucleus (Figure 8B), consistent with the observation of reduced levels of transcription and translation under stress.[24] Differentially downregulated genes in SD are uniquely enriched in amino acid transport, cell cycle, protein glycosylation, and drug transmembrane transport (Figure 8B).

Enrichment of MF GO terms in each encapsulation method is arranged into clusters and shown in Figure 9. Upregulated genes

DOI: 10.1021/acsnano.6b06385
ACS Nano 2017, 11, 3560−3575

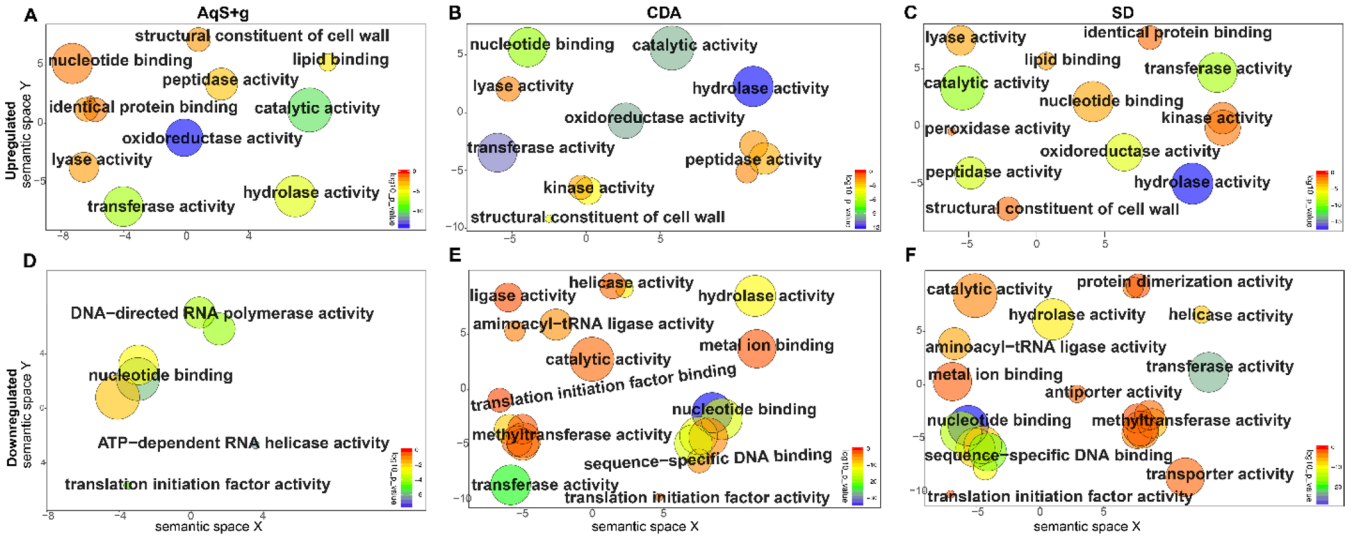

Figure 9. GO enrichment of MF terms as determined according to the DAVID. Redundant GO terms were removed and then summarized by REVIGO and represented as a scatter plot. (A−C) Upregulated molecular functions for *S. cerevisiae* encapsulated *via* (A) AqS+g, (B) CDA, and (C) SD. (D−F) Downregulated molecular functions for *S. cerevisiae* encapsulated *via* (D) AqS+g, (E) CDA, and (F) SD. GO terms are shown by circles and plotted by semantic similarity with other GO terms; circles closer to each other show closely related GO terms. The size of the circle is relative to the frequency of the GO term in the underlying GO database. Circle color represents the log 10 *p*-values. GO terms with B&H corrected *p*-values <0.05 are shown.

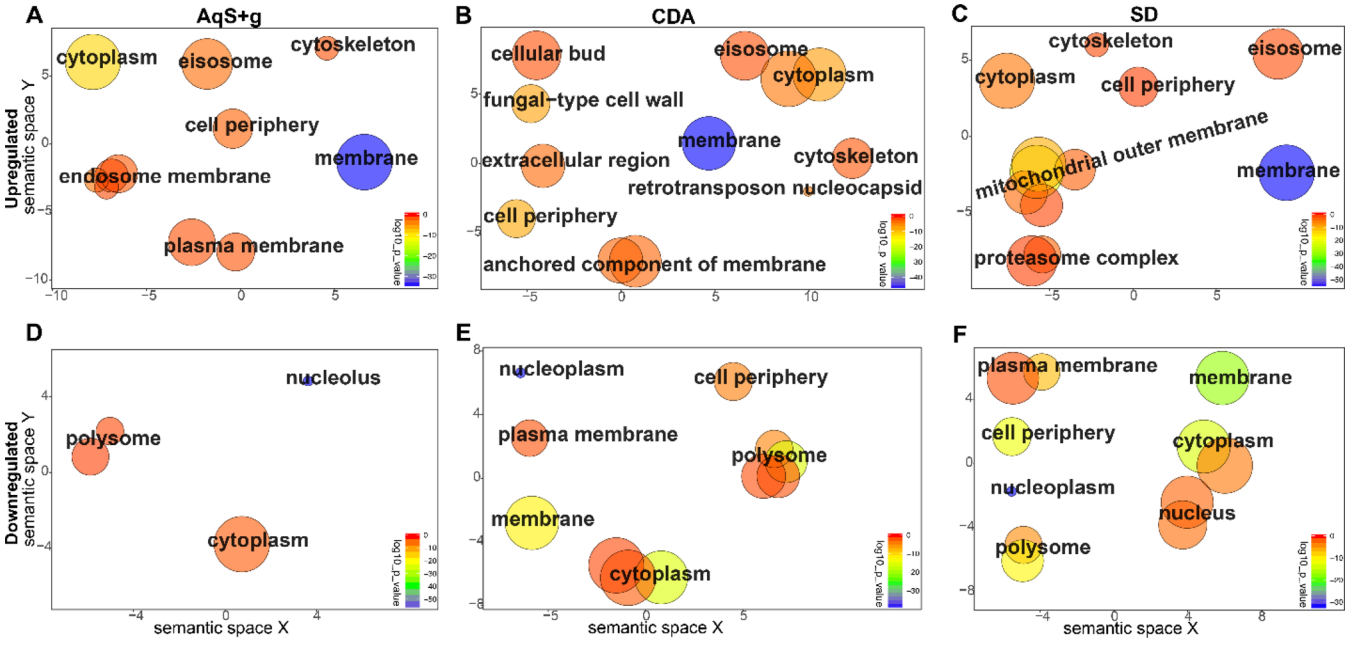

Figure 10. GO enrichment of CC terms as determined according to the DAVID. Redundant GO terms were removed and then summarized by REVIGO and represented as a scatter plot. (A−C) Upregulated cellular components for *S. cerevisiae* encapsulated *via* (A) AqS+g, (B) CDA, and (C) SD. (D−F) Downregulated cellular components for *S. cerevisiae* encapsulated *via* (D) AqS+g, (E) CDA, and (F) SD. GO terms are shown by circles and plotted by semantic similarity with other GO terms; circles closer to each other shows closely related GO terms. The size of the circle is relative to the frequency of the GO term in the underlying GO database. Circle color represents the log 10 *p*-value. GO terms with B&H corrected *p*-values <0.05 are shown.

in all three methods are enriched in oxidoreductase activity, lyase activity, peptidase activity, and structural constituents of cell wall terms (Figure 9A−C). Upregulation of oxidoreductase activity is consistent with upregulation of the BP term response to oxidative stress enriched in all three methods (Figure 7A−C). Downregulated genes from all three methods are enriched in translation initiation factor activity (Figure 9D−F). Both upregulated and downregulated genes from all three methods are enriched in nucleotide binding (Figure 9A−F). Downregulated clusters of aminoacyl-tRNA ligase, metal ion binding, and sequence-specific DNA binding are only enriched in CDA and SD (Figure 9E,F). Ligase activity and translation initiation factor binding are uniquely enriched in downregulated genes in the CDA method (Figure 9E). Transporter activity and antiporter activity are uniquely enriched in downregulated genes in the SD method (Figure 9F). A detailed list of unique

DOI: 10.1021/acsnano.6b06385
ACS Nano 2017, 11, 3560−3575

differentially upregulated and downregulated MF terms in each method is displayed as a heat map in Supplemental Figure S4.

Enrichment of CC GO terms in each encapsulation method is shown in Figure 10. The upregulated gene lists from all three methods are enriched in eisosome, cytoskeleton, and membrane terms (Figure 10A–C). Furthermore, upregulated and downregulated genes in all three methods are enriched in cytoplasm and polysome terms (Figure 10A–F). Upregulated genes in SD and AqS+g are both enriched in proteasome complex (Figure 10C and Supporting Information File 2, respectively). The downregulated genes in both CDA and SD are downregulated enriched in nucleoplasm and plasma membrane (Figure 10E, F). In contrast to the SD and AqS+g gene sets, the upregulated genes in CDA method are enriched in the CC categories fungal-type cell wall, extracellular region, and anchored component of membrane terms (Figure 10B). These are consistent with cell wall-associated observations in the BP enriched GO terms in the same (CDA) method (Figure 7B). Furthermore, the CC term "cellular bud" is only enriched in cells encapsulated by the CDA method (Figure 10B). A detailed list of unique differentially upregulated and downregulated CC terms in each method is displayed as a heatmap in Supplemental Figure S5.

Enriched Kyoto Encyclopedia of Genes and Genomes (KEGG) pathways (to a p-value of <0.01) are shown for upregulated and downregulated genes for each encapsulation method in Tables 1 and 2, respectively. For all three encapsulation methods, metabolic pathways, biosynthesis of secondary metabolites, endocytosis, carbon metabolism, peroxisome, regulation of autophagy, and protein processing in endoplasmic reticulum are enriched in upregulated genes. Upregulated genes of AqS+g are uniquely enriched in fatty acid degradation, pyruvate metabolism, biosynthesis of amino acids, and tryptophan metabolism pathways. Upregulated genes of SD are uniquely enriched in proteasome and methane metabolism pathways. In the case of CDA, upregulated genes are uniquely enriched in meiosis, starch and sucrose metabolism, and phosphatidylinositol signaling system pathways.

Table 1. Enriched Pathways in Upregulated Genes in Each Encapsulation Method

pathway name	B&H corrected p-value		
	CDA	AqS+g	SD
metabolic pathways	5.33×10^{-20}	5.33×10^{-17}	3.32×10^{-23}
biosynthesis of secondary metabolites	5.04×10^{-10}	1.25×10^{-12}	1.89×10^{-13}
endocytosis	4.63×10^{-5}	8.79×10^{-12}	5.97×10^{-8}
carbon metabolism	1.17×10^{-6}	6.51×10^{-7}	2.30×10^{-7}
peroxisome	5.32×10^{-5}	8.58×10^{-7}	4.74×10^{-7}
protein processing in endoplasmic reticulum	4.22×10^{-5}	1.78×10^{-4}	5.60×10^{-5}
glycerolipid metabolism	>0.01	1.99×10^{-4}	1.94×10^{-4}
fatty acid degradation	>0.01	5.31×10^{-4}	>0.01
pyruvate metabolism	>0.01	9.05×10^{-4}	>0.01
SNARE interactions in vesicular transport	>0.01	0.0011	9.82×10^{-4}
regulation of autophagy	3.54×10^{-5}	0.0011	1.07×10^{-4}
glycolysis/gluconeogenesis	0.0016	0.0025	>0.01
biosynthesis of amino acids	>0.01	0.0027	>0.01
tryptophan metabolism	>0.01	0.0065	>0.01
proteasome	>0.01	>0.01	2.46×10^{-5}
methane metabolism	>0.01	>0.01	0.0068
glycerophospholipid metabolism	0.0032	>0.01	0.0035
meiosis	3.38×10^{-6}	>0.01	>0.01
starch and sucrose metabolism	9.77×10^{-6}	>0.01	>0.01
phosphatidylinositol signaling system	0.0066	>0.01	>0.01

Table 2. Enriched Pathways in Downregulated Genes in Each Encapsulation Method

pathway name	B&H corrected p-value		
	CDA	AqS+g	SD
ribosome biogenesis in eukaryotes	3.25×10^{-26}	6.96×10^{-24}	1.50×10^{-25}
metabolic pathways	4.77×10^{-22}	8.16×10^{-13}	2.60×10^{-20}
pyrimidine metabolism	3.11×10^{-12}	1.27×10^{-9}	2.21×10^{-11}
purine metabolism	3.49×10^{-12}	6.84×10^{-8}	1.00×10^{-8}
RNA transport	1.85×10^{-14}	2.66×10^{-6}	2.13×10^{-8}
aminoacyl-tRNA biosynthesis	1.25×10^{-4}	1.10×10^{-5}	1.00×10^{-4}
RNA polymerase	2.04×10^{-9}	5.11×10^{-4}	2.35×10^{-8}
biosynthesis of secondary metabolites	1.40×10^{-7}	5.55×10^{-4}	1.41×10^{-7}
biosynthesis of amino acids	4.65×10^{-8}	5.72×10^{-4}	2.26×10^{-10}
phenylalanine, tyrosine and tryptophan biosynthesis	>0.01	0.0027	0.0022
cell cycle - yeast	0.0034	>0.01	3.45×10^{-4}
RNA degradation	4.23×10^{-5}	>0.01	>0.01
ribosome	2.70×10^{-4}	>0.01	>0.01
2-oxocarboxylic acid metabolism	0.0017	>0.01	0.0015
cysteine and methionine metabolism	0.0023	>0.01	5.70×10^{-4}
spliceosome	0.0029	>0.01	>0.01
alanine, aspartate and glutamate metabolism	0.0052	>0.01	0.0070
arginine biosynthesis	0.0084	>0.01	>0.01
mRNA surveillance pathway	0.0089	>0.01	>0.01
meiosis - yeast	>0.01	>0.01	7.27×10^{-6}
glycine, serine, and threonine metabolism	>0.01	>0.01	5.63×10^{-4}
MAPK signaling pathway - yeast	>0.01	>0.01	0.0025

In the case of downregulated genes, ribosome biogenesis in eukaryotes, metabolic pathways, pyrimidine metabolism, purine metabolism, RNA transport, aminoacyl-tRNA biosynthesis, RNA polymerase, biosynthesis of secondary metabolites, and biosynthesis of amino acids are enriched in all three methods. Downregulated genes of CDA are uniquely enriched in RNA degradation, ribosome, spliceosome, arginine biosynthesis, and the mRNA surveillance pathway. Downregulated genes in SD are uniquely enriched in meiosis, glycine, serine, and threonine metabolism, and the MAPK signaling pathway. A more extensive table showing all enriched pathways at p-value <0.05 is provided in Supporting Information File 2. Additionally, differentially expressed genes from each encapsulation method are graphically overlaid on highly enriched KEGG pathways at p-value <0.001 (from Tables 1 and 2) to show at what specific pathway stage/process the differentially expressed genes are involved (Supplemental Figures S8–S47).

Unique Metabolic States for Encapsulated *S. cerevisiae* Cells. These enrichment results provide substantial new insight and understanding regarding the physiological state of living cells confined within silica matrices. Each of the three matrices studied in this work induced a unique metabolic state in the encapsulated

DOI: 10.1021/acsnano.6b06385
ACS Nano 2017, 11, 3560–3575

S. cerevisiae cells. Significant overlap in gene expression profiles was observed between CDA and SD entrapment methods, which may be expected as both methods employ identical silica-lipid sol precursor solution chemistry. Still, substantial differences in gene expression profiles between the two methods were observed. In the case of CDA, cell wall processes were uniquely upregulated. This indicates that of the three encapsulation methods, cells entrapped *via* CDA experience greater cell wall associated stresses. This may be a result of the higher exposure time of these cells to the precursor sol solution, which contains ethanol, acid, and hydrolyzed silica particles that may interact with, or pass through, the cell wall and stress or damage the cell. *S. cerevisiae* cells use the cell wall integrity (CWI) pathway to maintain cell wall integrity and repair damage *via* cell wall biosynthesis and actin organization.[56] The cell wall integrity pathway also cross-talks to other cell stress pathways to relieve stresses.[57] Cells entrapped *via* CDA also showed substantial reduction in gene expression associated with ribosome biosynthesis and RNA processing. Biosynthetic processes require considerable energy and reduced expression of rRNA processing, and ribosome biogenesis indicates that the cells are under stress and are minimizing energy consumption.

For cells encapsulated *via* the SD process, fatty acid beta oxidation GO term was very highly enriched (B&H corrected p-value = 0.0000182) in upregulated genes. The upregulation of these terms indicates that in the absence of a carbon nutrient source, *S. cerevisiae* cells can generate energy from the oxidation of fatty acids present in the encapsulation matrix at the cell surface. This results in acetyl moieties that can be used in the TCA cycle for generation of energy through anabolic metabolism. Interestingly, oxidation of fatty acids occurs in peroxisomes of *S. cerevisiae* cells,[58] and this is in agreement with the upregulated CC GO peroxisomal matrix term (Supporting Information File 2). As indicated previously and as observed in previous reports, our results suggest that there is a lipid interface between the cell and the surrounding lipid-templated matrix which may offer the cell a source of nutrients. We previously showed using a fluorescence recovery after photobleaching assay that this lipid layer is interdigitated throughout the entire bulk of CDA thin films and SD particles, and it remains extremely fluid. Thus, encapsulated cells are presented with a replenishing source of fatty acid nutrients even in the dry particle state. The SD method entrapped cells also show significant reduction in ribosomal biogenesis and rRNA processing, indicating that the cells are under stress, but not to the same extent as cells entrapped *via* CDA. This may allow for some metabolic load to be focused on lipid metabolism for energy generation.

Overall, AqS+g cells exhibited fewer differentially expressed genes and fewer differentially expressed GO terms than either CDA or SD, indicating that this encapsulation method induced less drastic disruption than either SD or CDA. In particular, *S. cerevisiae* AqS+g cells lacked stress-related terms exhibited by CDA, or SD, or both including: upregulated lipid and carbohydrate metabolism such as observed in CDA and SD, upregulated cell wall organization and downregulation of mRNA transport, mRNA processing, nucleoside metabolism, and mitophagy observed in CDA. Furthermore, AqS+g cells use ubiquitin-dependent protein catabolism, while SD cells use proteasomal machinery for protein catabolism (*i.e.*, ubiquitin-independent protein catabolism) along with ubiquitin-dependent protein catabolism. Overall, by the measure of stress-related enriched GO categories, the AqS+g method encapsulated cells are less stressed than cells entrapped *via* CDA or SD. We believe one reason is the inclusion of glycerol in AqS+g matrix, which is known to enhance long-term cellular viability.[20] This is attributed to the formation of a high glycerol and water containing region between the cells and the surrounding nanostructured silica matrix, resulting in a fluid interface between the cell membrane and polar silanol groups that may damage the membrane, while also insulating the cell from stresses induced during gelation.[19,33] We further believe that *S. cerevisiae* cells encapsulated in AqS+g can use glycerol as a source of carbon nutrient.[59]

Quiescent states in *S. cerevisiae* are commonly induced by stress, such as starvation, anoxia, *etc.*[47] These states are generally characterized by downregulation of genes associated with many forms of biosynthesis, but an upregulation of genes associated with forms of maintenance, for example, cell wall maintenance.[60] Within this general framework, we note that *S. cerevisiae* does not exhibit one, but rather several different quiescent states depending on the particular stress that induced the state (starvation of a particular nutrient, for example).[60] Gene expression patterns were further analyzed and compared to known, naturally occurring metabolic states. Major states identified in the literature include exponential growth, stationary, quiescent, dormancy, and persister.[47,61,62] It is difficult to distinguish between the states that various authors describe as quiescence, dormancy, and persistence, to the extent that it may be reasonable to consider them different names for the same entity. In the remainder of this paper we will adopt the term "quiescence," not because we prefer it to the other two, but simply to have one label.

The gene expression patterns induced by all three methods are generally consistent with the pattern of quiescence, but as with other stresses, there are differences in the details of the quiescent states. The above-mentioned major shifts of gene expression we see in encapsulated cells relative to the unencapsulated stationary state are characteristic of the quiescent state. In general, quiescent states are phenotypic variants of wild-type cells and are induced by stresses such as nutrient starvation, antifungal stress, or induction of biofilm formation.[63] Under conditions of high nutrient availability, the TOR complex 1 (TORC1) pathway plays an important role in cell growth by positively regulating ribosome biogenesis and inhibiting stress associated pathways that have negative effects on cell growth such as CWI pathways.[56] However, under a stress environment or as a response to the unavailability of nutrients, TORC1 is inhibited, resulting in no cell growth, one characteristic of a quiescent state.[64] Bojsen *et al.*[63] recently reported that inhibition of TORC1 in *S. cerevisiae* resulted in increased tolerance to antifungal agents.

Significance of Confinement and the Bio−Nano Interface on Living Cell Metabolic State. While confinement within silica matrices has been widely reported to induce significant and unexpected shifts in biological behaviors, a comprehensive understanding of the influence encapsulation matrix properties has on specific biological functions is lacking. In this first analysis of how systematic modifications of the encapsulating nanostructure influence *S. cerevisiae* cells genetic expression profiles, it is clear that the physicochemical properties at the bio−nano interface influence the metabolic state of encapsulated cells beyond those induced by 3D physical confinement alone. This is evidenced by uniquely enriched genes and associated unique functional categories from each method. As shown in the heat map and Venn diagram in Figure 5, 750 upregulated and 598 downregulated genes are shared between all three encapsulation chemistries. However, and importantly, there are a similar

DOI: 10.1021/acsnano.6b06385
ACS Nano 2017, 11, 3560−3575

number of unshared up and downregulated genes among each encapsulation method (AqS+g: 444 up, 344 down; CDA: 565 up, 786 down; SD: 707 up, 694 down). This is also shown in Figure 8 and in Supplemental Figures S4 and S5. Physicochemical properties at the bio−nano interface are also more influential than the overall chemistry of the confinement matrix. Although both CDA and SD methods employ identical matrix chemistries and share many enriched genes (936 upregulated, 902 downregulated), many genes were still uniquely enriched by the two methods (CDA: 379 up, 482 down; SD: 521 up, 390 down). Overall, of the 3872 differentially regulated genes measured in this study, 1508, or 39%, were unique to a given encapsulation matrix, demonstrating that the interaction of the cell with the three differing nanostructures substantially impacts cell metabolism.

Here it is noteworthy that the three different encapsulating matrices were all amorphous silicate-based. There is a large body of work studying the toxicity of nanostructured materials, which has been shown to differ from the toxicity of bulk materials of the same chemical composition. That work shows that the nanostructure and type of nanomaterial clearly influence cellular metabolic activity. From data collected in this study, any silica-specific effects on the metabolic state of the cells is challenging to determine. Still, it is known that amorphous silica materials are generally recognized as safe by the U.S. Food and Drug Administration and that sol−gel derived silica nanoparticles have been FDA approved for diagnostic applications in a stage I human clinical trial.[65] It is therefore unlikely that there would be significant silica-specific toxicity or effects on cell metabolism. In the case of CDA *versus* SD, the starting lipid/silica compositions were identical, the physicochemical properties at the bio−nano interface differed significantly. This includes differences in the physical interaction of lipid, glycerol, and silica with the cell wall, as shown in the TEM imaging data (Figures 2−4). Also, physical forces exerted at the bio−nano interface differ between each matrix, as indicated by mechanical modulus data. As we recently reported, the Young's modulus of SD matrices is ∼14 GPa, as determined by nanoindentation, compared to ∼4 GPa for CDA determined in an identical manner.[36] Due to their porosity (see Figure 4), aqueous silica gel matrices are much softer. Based on literature reports, we estimate the Young's modulus of the AqS+g matrix to be from ∼500 KPa to 2 MPa[42] (where Young's modulus, E, is calculated from the reported shear modulus, G, by $E = 2(1 + n)\,G$, where Poisson's ratio n is assumed to be 0.2), over 1000× softer than SD. Thus, these differing matrices mechanically constrain the cell to differing extents, which could be manifested in multiple stress-associated pathways. Although the aqueous gels are quite soft, they still inhibited replication of *S. cerevisiae* as did the stiffer, conformal CDA and SD matrices. This is in contrast to very soft silica gel matrices or hierarchical macro-meso-microporous silica gels where replication of *E. coli* was observed, respectively.[29,34]

Therefore, when using materials chemistry to elicit a desired biological response, the bio−nano interface structural and chemical properties are highly significant parameters to control. This understanding opens the possibility of integrating living cells within functional materials that are less biocompatible, or even cytotoxic, but may provide long-term viability and activity by incorporating a well-designed bio−nano interface. Finally, tuning the parameters of the bio−nano interface can induce yet unexplored cellular states that will require further study to understand, but may contribute substantial understanding of cancer, aging, cell signaling, quorum sensing, starvation, and other complex cellular behaviors.

CONCLUSION

In summary, we have performed a comprehensive genetic analysis of living cells encapsulated within silica matrices. Comparison of encapsulated cells RNA levels with stationary phase cells permitted the identification of stresses exerted on the cells associated with a given encapsulation chemistry and a broad data set illustrative of the cells' metabolic processes. This will allow for further tuning of the given encapsulation approach to improve upon the desired biological traits, enhancing the performance of the hybrid biomaterial. This study also showed that the material properties at the bio−nano interface significantly influence biological behavior, in addition to the bulk chemistry of the matrix and physical confinement alone. Distinct metabolic states for cells entrapped in each silica matrix were observed. In future work, we believe it will be possible to induce, and perhaps control, a particular biological state by tuning the nanomaterial properties at the bio−nano interface of the encapsulation matrix. This ability may provide a powerful new technique for the study of complex cellular behaviors impacting the fields of cancer, aging, cell−cell signaling and quorum sensing research and the development of bioelectronics and cell-based biosensors.

MATERIALS AND METHODS

Materials. *Saccharomyces cerevisiae* (strain S288c) was acquired from American Type Culture Collection (ATCC; Manassas, VA). 1,2-Dihexanoyl-*sn*-glycero-3-phosphocholine (diC_6PC) was purchased from Avanti Polar Lipids, Inc. (Alabaster, AL). Absolute ethanol, hydrochloric acid (HCl, 37%), tetraethylorthosilicate (TEOS, 98%), sodium silicate solution (26.5% SiO_2; 10.6% Na_2O), strongly acid cation-exchange resin (DOWEX 50WX8-100, hydrogen, 50−100 mesh), glycerol, yeast extract, peptone, D-(+)-glucose, adenine, sodium acetate, ethylenediaminetetraacetic acid (EDTA), sodium dodecyl sulfate (SDS), phenol, choloroform:isoamyl alcohol (24:1), sodium phosphate (mono- and dibasic), sodium acetate, phosphate buffer saline (PBS, pH 7.0), glass beads, and Alconox detergent were purchased from Sigma-Aldrich (St. Louis, MO). RNeasy Mini Kit (including Buffer RW1 and Buffer RPE) was obtained from Qiagen (Germantown, MD). RNA 6000 Nano Kit was purchased from Agilent (Santa Clara, CA). Yeast Genome 2.0 Arrays and Genechip 3′ IVT Express Kits were purchased from Affymetrix (Santa Clara, CA).

Cell Culture. *S. cerevisiae* S288c cells were grown aerobically in yeast peptone dextrose + adenine (YPD+A) broth at 30 °C for 7 days until the culture was in stationary phase (OD600 1.5−2.0). Cells were then centrifuged at 10,000 rpm for 5 min, washed with DI H_2O three times, and resuspended in DI H_2O (OD600 0.1−1.0).

Encapsulation of *S. cerevisiae* in Phospholipid-Templated Silica Films *via* CDA.[40] Glass coverslips (25 mm, No. 1.5) were soaked in 0.1 M KOH for a minimum of 4 h, washed with 10% Alconox (m/v), rinsed with DI H_2O, dried under a stream of N_2 gas, and then cleaned in UV-ozone (Jelight, model 342) for 5 min. Prehydrolyzed TEOS stock solutions (A2**) were made by refluxing 61 mL of TEOS, 61 mL of absolute ethanol, 4.9 mL of DI H_2O, and 0.2 mL of 0.07 N HCl (molar ratio $1:4:1:5 \times 10^{-5}$) for 90 min at 60 °C. A2** stock solutions were then stored at −20 °C. CDA precursor sol was prepared by combining 0.25 mL of A2** stock solution, 0.2 mL of absolute ethanol, 0.16 mL of 0.05 N HCl, 0.4 mL of DI H_2O, and 30 mg of diC_6PC. This precursor solution was aged at room temperature for 20 min and then passed through a 0.45 μm filter. To this solution was combined an equal volume of PBS washed and resuspended *S. cerevisiae*. This mixture was cast onto cleaned glass coverslips. Resulting thin films were allowed to air dry, rinsed with DI H_2O to remove nonintegrated cells, and stored under ambient conditions (25 °C ± 2 °C) for 3 days.

DOI: 10.1021/acsnano.6b06385
ACS Nano 2017, 11, 3560−3575

Encapsulation of *S. cerevisiae* in Phospholipid-Templated Silica Particles *via* SD.[36] The silica precursor sol was prepared by adding 0.83 mL A2** stock (described above) to a solution containing 1.33 mL of DI H_2O, 0.66 mL of ethanol, and 0.53 mL of 0.07 N HCl; the same chemistry as the CDA method, but scaled-up for higher material yield. This solution was allowed to age at room temperature with sonication for 30−60 min until complete homogenization of the precursors had occurred. Immediately prior to sample preparation, 100 mg of diC_6PC lipid was added to the fully condensed sol and mixed until fully dissolved (~20 s).

Samples were spray dried with a Mini Spray Drier B-290 (Buchi, Flawil, Switzerland) using a 0.7 mm nozzle. The inlet temperature of the spray nozzle was adjusted between 60 and 65 °C to maintain an outlet temperature of 30 °C, with an aspiration rate of 90%, a peristaltic pump feed rate of 3.5 mL/min, and nitrogen as a carrier gas at a rate of 60 L/h. 3.3 mL of precursor sol and dissolved lipid (described above) and 3.3 mL of cells in PBS suspension were loaded into separate assimilation vials. Two peristaltic pumps with individual feed rates of 1.75 mL/min (3.5 mL/min combined feed rate) were used to deliver the solution to the spray drier nozzle with mixing *via* a Y connector immediately prior to inspiration into the nozzle. This technique allowed for minimal contact between cells and the acidic and alcoholic precursor solution, improving cell viability. After mixing, the solution containing cells, silica precursors, and lipid was aerosolized into the dry nitrogen sheath established within the spray drier. Rapid evaporation of the solvent results in lipid-directed EISA. Particles are fully dried before entering the spray drier cyclone. Spray dried particles were collected in assimilation vials that were connected to the standard cyclone, replacing the standard collection chamber. After SD, samples were stored under ambient conditions (25 °C ± 2 °C and 60% RH ± 5% RH) for 3 days.

Encapsulation of *S. cerevisiae* in AqS+g.[39] An aqueous silica matrix precursor solution was prepared by adding 1.654 mL of sodium silicate solution to 6.8 mL of DI H_2O. This mixture was immediately added to 3.08 g of highly acidic hydrogen (H^+) cation-exchange resin. The solution was mixed for approximately 2 min. The resin was then removed by vacuum filtration or by centrifugation to pellet the resin, followed by collection of the supernatant. To this solution, 20% (vol.) glycerol was added. Stationary phase *S. cerevisiae* cells were washed 3× and resuspended in 1.0 M sodium phosphate buffer, pH 7.0. Cells in buffer and aqueous sol precursor solution were then mixed in a 1:1 ratio. Gelation occurred within 25−30 s of mixing the two solutions. Final cell density was 10^6−10^7 cells/mL. Silica gels were formed and stored under ambient conditions (25 °C ± 2 °C) for 3 days.

Optical Microscopy. For optical imaging, dried powders were suspended in water, vortexed for 10s, and pipetted onto standard microscope slides. Samples were imaged on a Zeiss LSM 510 confocal microscope mounted on a Zeiss Axiovert 100 inverted microscope. Prior to encapsulation, *S. cerevisiae* was stained with Syto-9 green fluorescent dye according to manufacturer's specifications.

We created z-stack images for particles of varying sizes in order to visualize the distribution of cells within particles. This was achieved by setting the upper and lower boundaries of a particle and taking an image with a given optical slice diameter and collecting an image every diameter distance. The resulting collection of images maps the entire z-dimension within the sample, allowing us to create 3D reconstructions of the sample. Compressed z-stack images were created by merging all of the images from the z-stack into one image, allowing for easier visualization of the entire particle.

Electron Microscopy. Prior to TEM, image contrast between *S. cerevisiae* cells and the encapsulating matrix was improved for all three matrix types *via* fixation and staining of cells using glutaraldehyde and osmium tetroxide, respectively. For CDA and SD samples, this was accomplished simply by adding the powder to the solutions outlined below. For the gel sample, a cured gel (300 μL volume, *vida infra*) was fractured into smaller ~1 mm pieces using a clean razor blade prior to treatment. We fixed the cells by incubating the samples in 2.5% glutaraldehyde in PBS for 1 h at room temperature followed by 3× rinse cycles in PBS using 10k RPM and 30s for centrifuge settings. We stained the samples using osmium tetroxide (OsO_4), following the protocol recommended by R. Wright.[66] Here, fixed cells are centrifuged, the supernatant is removed, 1% OsO_4 in PBS is added, and the sample is incubated for 2 h on ice due to the high vapor pressure of OsO_4.

Prior to TEM imaging, it was necessary to remove the aqueous phase within the samples, which was done by stepwise dehydration and water replacement with ethanol. This was achieved by incubating the three fixed and stained samples in increasing concentrations of EtOH for 15 min (concentrations were 30%, 50%, 70%, and 90%) and finally for 60 min (concentrations were 95% and 100%). Dehydrated samples were stored at 4 °C. For TEM imaging, samples were switched to an anhydrous acetone for the final dehydration. The preparation was then infiltrated with resin by incubating particles in 1:1 Spurr's resin:acetone, 3:1 Spurr's resin:acetone, and, finally, 100% Spurr's resin. Samples were placed in embedding molds and polymerized by incubation at 60 °C for at least 16 h, and the blocks were trimmed for microtoming. Microtomed sections with thicknesses between 60 and 80 nm were used for imaging. Transmission electron microscopy was performed using a Hitachi H7700 equipped with an AMT XR16 M 16 megapixel camera.

Extraction and Purification of RNA from Encapsulated Cells. Portions of encapsulated cell-containing silica matrices were rinsed with DI H_2O and placed in 2 mL centrifuge tubes, breaking the matrix into smaller pieces as necessary. 270 μL of sodium acetate buffer (50 mM of sodium acetate, pH 5.2, and 10 mM of EDTA, pH 8.0), 30 μL of 10% SDS, and approximately 100 μL of glass beads (0.5−0.6 mm diameter) were added to centrifuge tubes. Samples were stirred and agitated to physically break apart the matrix. Water-saturated acid phenol (300 μL) preheated to 65 °C was added to the samples, followed by vortexing for 1 min. Samples were then incubated in a 65 °C water bath for 5 min, followed again by vortexing for 1 min. This was repeated for a total of six cycles over approximately 45 min. Samples were then placed in a cooling block for 2 min, followed by the addition of 300 μL chloroform:isoamyl alcohol (24:1), and mixed by vortexing for 30 s. Samples were then centrifuged for 5 min at 15,000 rpm, followed by transferring the RNA-containing top layer to new centrifuge tubes. An equal volume of 70% ethanol was added and mixed by pipetting.

Next, samples were transferred to Qiagen RNeasy spin columns and centrifuged for 30 s at 15,000 rpm, discarding flow through. 700 μL of RW1 buffer was added to the columns, and the samples were centrifuged for 30 s at 15,000 rpm, discarding flow through. 500 μL of RPE buffer was added to the columns, followed by centrifugation for 30 s at 15,000 rpm, discarding flow through. 500 μL of RPE buffer was added to the columns, followed by centrifuging for 2 min at 15,000 rpm, discarding flow through. Columns were then placed in new 2 mL collection tubes and centrifuged for 1 min at 15,000 rpm. Next, columns were placed in new 1.5 mL collection tubes, and 40 μL of DI H_2O was added. Columns were again centrifuged for 1 min at 15,000 rpm, after which 40 μL of DI H_2O was added, and the columns were centrifuged again for 1 min, yielding the purified RNA product. A NanoDrop spectrophotometer (Wilmington, DE) and an Agilent 2100 Bioanalyzer (Santa Clara, CA) were used to determine concentration, purity, and integrity of RNA extractions. RNA samples were stored at −20 °C until used.

Gene Chip Hybridization. cDNA preparation and biotin-labeled cRNA generation and fragmentation were performed using Affymetix Genechip 3′ IVT Express Kits per the manufacturers protocol. Hybridization solution was prepared with the fragmented cRNA and controls and was then hybridized to the probe array with a 16 h incubation period. The solution was then removed, and the probe array was washed and stained in an automated microfluidics station. Arrays were read by an Affymetrix GeneChip Scanner attached to a workstation running Affymetrix Microarray Suite.

Experimental Design. Gene chip data from four treatment groups were collected. Each treatment had two replicates. Group 1: Stationary phase *S. cerevisiae* cells (grown for 7 days in aerated media) washed and resuspended in phosphate buffer saline solution (PBS). This group served as the baseline cultured *S. cerevisiae* control to which the RNA expression levels from sample groups 2−4 were compared. Group 2: Stationary phase *S. cerevisiae* cells encapsulation in silica *via* CDA and stored dry for 3 days under ambient temperature and relative humidity (RH). Group 3: Stationary phase *S. cerevisiae* cells encapsulation in silica *via* SD and stored dry for 3 days under ambient temperature and RH.

DOI: 10.1021/acsnano.6b06385
ACS Nano 2017, 11, 3560−3575

Group 4: Stationary phase *S. cerevisiae* cells encapsulation in glycerol-doped aqueous silica gels and stored sealed for 3 days under ambient temperature.

Identification of Differentially Expressed Genes. Statistical analyses were performed with the LIMMA[67] R package using an empirical Bayes linear modeling approach, and gene expression intensities were normalized using GeneChip RMA (GCRMA)[68] normalization. To control multiple hypothesis testing, the B&H[49] method was used to correct raw *p*-values. The resulting statistical analyses provide the differentially expressed genes with respect to control based on estimate measures of gene expression, with associated *p*-values. The B&H corrected *p*-value <0.05 and log 2-fold change (log2FC) of >1 and <−1 was used to identify the upregulated and downregulated genes, respectively. Cluster 3.0[69] program was used to do hierarchical clustering with complete linkage, and Euclidean distance was used as distance similarity metric. The resulting cluster was visualized using Java TreeView program.[70]

Identification of Functional GO Terms and KEGG Pathways Overrepresented in Differentially Expressed Genes. The DAVID[50] was used to identify enriched GO terms. This functional analysis permitted the identification of GO[48] from the gene expression data, including BP, CC, and MF. GO terms were considered significantly enriched at B&H corrected *p*-value <0.05 using the Yeast 2.0 array as background. Redundant GO terms were removed and further summarized by semantic similarity in REVIGO[51] and represented by two-dimensional space in scatter plots. The GO terms that are semantically similar should position together in a scatter plot, and semantic space units have no inherent meaning. The size of the circle is relative to the frequency of the GO term in underlying GO database; however, the color of circle represents the log 10 *p*-value. GO terms with B&H corrected *p*-value <0.05 are shown on scatter plots. The threshold used for allowed sematic similarity is "medium". KEGG[71] pathway enrichment analysis was carried out using the DAVID[50] to find significant pathways overrepresented in different encapsulation methods. The KEGG pathways were considered significantly enriched at a B&H corrected *p*-value <0.05 using Yeast 2.0 background.

ASSOCIATED CONTENT

Supporting Information

(1) The Supporting Information is available free of charge on the ACS Publications website at DOI: 10.1021/acsnano.6b06385.

Fluorescence data verifying cellular encapsulation as well as detailing the general cell loading densities and cell placement within CDA thin films, SD powders, and AqS+g gel monoliths (PDF)

Complete list of biological processes, molecular functions, and cellular components GO terms enriched in all three methods of encapsulation (XLSX)

AUTHOR INFORMATION

Corresponding Authors

*E-mail: jake@illinois.edu.

*E-mail: cjbrink@sandia.gov.

ORCID

Eric Jakobsson: 0000-0002-7892-5295

Notes

The authors declare no competing financial interest.

ACKNOWLEDGMENTS

We would like to thank Dr. Stephen Jett in the University of New Mexico Health Sciences Center for help with TEM sample preparation and image collection. TEM data were generated in the UNM Electron Microscopy Shared Facility supported by the University of New Mexico Health Sciences Center and the University of New Mexico Cancer Center. Fluorescence images in this paper were generated in the University of New Mexico and Cancer Center Fluorescence Microscopy Shared Resource, funded as detailed on: http://hsc.unm.edu/crtc/microscopy/acknowledgement.shtml. P.E.J. and J.P. acknowledge support from the Air Force Office of Scientific Research under grant no. FA9550-14-1-0066. C.J.B. acknowledges support from the U.S. Department of Energy, Office of Science, Basic Energy Sciences, Materials Sciences and Engineering Division for support of self-assembly of lipid/silica nanocomposites and the Sandia National Laboratory LDRD program for support of studies of cellular function. Sandia National Laboratory is a multiprogram laboratory operated by Sandia Corporation, a wholly owned subsidiary of Lockheed Martin Company, for the U.S. Department of Energy's National Nuclear Security Administration under contract DE-AC04-94AL85000.

REFERENCES

(1) Park, J. H.; Hong, D.; Lee, J.; Choi, I. S. Cell-in-Shell Hybrids: Chemical Nanoencapsulation of Individual Cells. *Acc. Chem. Res.* **2016**, *49*, 792−800.

(2) Orive, G.; Santos, E.; Poncelet, D.; Hernandez, R. M.; Pedraz, J. L.; Wahlberg, L. U.; De Vos, P.; Emerich, D. Cell Encapsulation: Technical and Clinical Advances. *Trends Pharmacol. Sci.* **2015**, *36*, 537−546.

(3) Ben-Yoav, H.; Melamed, S.; Freeman, A.; Shacham-Diamand, Y.; Belkin, S. Whole-Cell Biochips for Bio-Sensing: Integration of Live Cells and Inanimate Surfaces. *Crit. Rev. Biotechnol.* **2011**, *31*, 337−353.

(4) Ruiz-Hitzky, E.; Darder, M.; Aranda, P.; Ariga, K. Advances in Biomimetic and Nanostructured Biohybrid Materials. *Adv. Mater.* **2010**, *22*, 323−336.

(5) Leonard, A.; Dandoy, P.; Danloy, E.; Leroux, G.; Meunier, C. F.; Rooke, J. C.; Su, B.-L. Whole-Cell Based Hybrid Materials for Green Energy Production, Environmental Remediation and Smart Cell-Therapy. *Chem. Soc. Rev.* **2011**, *40*, 860−885.

(6) Burgain, J.; Gaiani, C.; Linder, M.; Scher, J. Encapsulation of Probiotic Living Cells: From Laboratory Scale to Industrial Applications. *J. Food Eng.* **2011**, *104*, 467−483.

(7) Meunier, C. F.; Rooke, J. C.; Léonard, A.; Xie, H.; Su, B.-L. Living Hybrid Materials Capable of Energy Conversion and CO 2 Assimilation. *Chem. Commun.* **2010**, *46*, 3843−3859.

(8) Carballeira, J. D.; Quezada, M. A.; Hoyos, P.; Simeó, Y.; Hernaiz, M. J.; Alcantara, A. R.; Sinisterra, J. V. Microbial Cells as Catalysts for Stereoselective Red−ox Reactions. *Biotechnol. Adv.* **2009**, *27*, 686−714.

(9) Harper, J. C.; Edwards, T. L.; Savage, T.; Harbaugh, S.; Kelley-Loughnane, N.; Stone, M. O.; Brinker, C. J.; Brozik, S. M. Orthogonal Cell-Based Biosensing: Fluorescent, Electrochemical, and Colorimetric Detection with Silica-Immobilized Cellular Communities Integrated with an ITO−Glass/Plastic Laminate Cartridge. *Small* **2012**, *8*, 2743−2751.

(10) Yap, F. L.; Zhang, Y. Protein and Cell Micropatterning and Its Integration with Micro/nanoparticles Assembly. *Biosens. Bioelectron.* **2007**, *22*, 775−788.

(11) Matsusaki, M.; Kadowaki, K.; Nakahara, Y.; Akashi, M. Fabrication of Cellular Multilayers with Nanometer-Sized Extracellular Matrix Films. *Angew. Chem.* **2007**, *119*, 4773−4776.

(12) Coradin, T.; Boissière, M.; Livage, J. Sol-Gel Chemistry in Medicinal Science. *Curr. Med. Chem.* **2006**, *13*, 99−108.

(13) Lee, K. Y.; Mooney, D. J. Alginate: Properties and Biomedical Applications. *Prog. Polym. Sci.* **2012**, *37*, 106−126.

(14) Drury, J. L.; Mooney, D. J. Hydrogels for Tissue Engineering: Scaffold Design Variables and Applications. *Biomaterials* **2003**, *24*, 4337−4351.

(15) Wang, S.; Guo, Z. Bio-Inspired Encapsulation and Functionalization of Living Cells with Artificial Shells. *Colloids Surf., B* **2014**, *113*, 483−500.

(16) Nassif, N.; Livage, J. From Diatoms to Silica-Based Biohybrids. *Chem. Soc. Rev.* **2011**, *40*, 849−859.

DOI: 10.1021/acsnano.6b06385
ACS Nano 2017, 11, 3560−3575

(17) Harper, J. C.; Khirpin, C. Y.; Carnes, E. C.; Ashley, C. E.; Lopez, D. M.; Savage, T.; Jones, H. D. T.; Davis, R. W.; Nunez, D. E.; Brinker, L. M.; et al. Cell-Directed Integration into Three-Dimensional Lipid–Silica Nanostructured Matrices. *ACS Nano* **2010**, *4*, 5539–5550.
(18) Conroy, J. F. T.; Power, M. E.; Martin, J.; Earp, B.; Hosticka, B.; Daitch, C. E.; Norris, P. M. Cells in Sol-Gels I: A Cytocompatible Route for the Production of Macroporous Silica Gels. *J. Sol-Gel Sci. Technol.* **2000**, *18*, 269–283.
(19) Ferrer, M. L.; Garcia-Carvajal, Z. Y.; Yuste, L.; Rojo, F.; del Monte, F. Bacteria Viability in Sol-Gel Materials Revisited: Cryo-SEM as a Suitable Tool to Study the Structural Integrity of Encapsulated Bacteria. *Chem. Mater.* **2006**, *18*, 1458–1463.
(20) Nassif, N.; Bouvet, O.; Rager, M. N.; Roux, C.; Coradin, T.; Livage, J. Living Bacteria in Silica Gels. *Nat. Mater.* **2002**, *1*, 42–44.
(21) Depagne, C.; Roux, C.; Coradin, T. How to Design Cell-Based Biosensors Using the Sol–gel Process. *Anal. Bioanal. Chem.* **2011**, *400*, 965–976.
(22) Nassif, N.; Roux, C.; Coradin, T.; Rager, M.-N.; Bouvet, O. M. M.; Livage, J. A Sol–gel Matrix to Preserve the Viability of Encapsulated Bacteria. *J. Mater. Chem.* **2003**, *13*, 203–208.
(23) Baca, H. K.; Carnes, E.; Singh, S.; Ashley, C.; Lopez, D.; Brinker, C. J. Cell-Directed Assembly of Bio/nano Interfaces—a New Scheme for Cell Immobilization. *Acc. Chem. Res.* **2007**, *40*, 836–845.
(24) Gasch, A. P.; Spellman, P. T.; Kao, C. M.; Carmel-Harel, O.; Eisen, M. B.; Storz, G.; Botstein, D.; Brown, P. O. Genomic Expression Programs in the Response of Yeast Cells to Environmental Changes. *Mol. Biol. Cell* **2000**, *11*, 4241–4257.
(25) Kültz, D. Molecular and Evolutionary Basis of the Cellular Stress Response. *Annu. Rev. Physiol.* **2005**, *67*, 225–257.
(26) Luscombe, N. M.; Babu, M. M.; Yu, H.; Snyder, M.; Teichmann, S. A.; Gerstein, M. Genomic Analysis of Regulatory Network Dynamics Reveals Large Topological Changes. *Nature* **2004**, *431*, 308–312.
(27) Cvitkovitch, D. G.; Li, Y. H.; Ellen, R. P. Quorum Sensing and Biofilm Formation in Streptococcal Infections. *J. Clin. Invest.* **2003**, *112*, 1626–1632.
(28) Carturan, G.; Monte, R. D.; Pressi, G.; Secondin, S.; Verza, P. Production of Valuable Drugs from Plant Cells Immobilized by Hybrid Sol-Gel SiO2. *J. Sol-Gel Sci. Technol.* **1998**, *13*, 273–276.
(29) Eleftheriou, N. M.; Ge, X.; Kolesnik, J.; Falconer, S. B.; Harris, R. J.; Khursigara, C.; Brown, E. D.; Brennan, J. D. Entrapment of Living Bacterial Cells in Low-Concentration Silica Materials Preserves Cell Division and Promoter Regulation. *Chem. Mater.* **2013**, *25*, 4798–4805.
(30) Blondeau, M.; Brayner, R.; Guyot, F.; Coradin, T. Correlating Biological Methods to Assess Escherichia Coli Bacteria Viability in Silica Gels. *Anal. Methods* **2014**, *6*, 2429–2431.
(31) Carnes, E. C.; Lopez, D. M.; Donegan, N. P.; Cheung, A.; Gresham, H.; Timmins, G. S.; Brinker, C. J. Confinement-Induced Quorum Sensing of Individual Staphylococcus Aureus Bacteria. *Nat. Chem. Biol.* **2010**, *6*, 41–45.
(32) Nassif, N.; Roux, C.; Coradin, T.; Bouvet, O. M. M.; Livage, J. Bacteria Quorum Sensing in Silica Matrices. *J. Mater. Chem.* **2004**, *14*, 2264–2268.
(33) Harper, J. C.; Lopez, D. M.; Larkin, E. C.; Economides, M. K.; McIntyre, S. K.; Alam, T. M.; Tartis, M. S.; Werner-Washburne, M.; Brinker, C. J.; Brozik, S. M. Encapsulation of S. Cerevisiae in Poly (Glycerol) Silicate Derived Matrices: Effect of Matrix Additives and Cell Metabolic Phase on Long-Term Viability and Rate of Gene Expression. *Chem. Mater.* **2011**, *23*, 2555–2564.
(34) Depardieu, M.; Viaud, M.; Buguin, A.; Livage, J.; Sanchez, C.; Backov, R. A Multiscale Study of Bacterial Proliferation Modes within Novel E. coli@Si(HIPE) Hybrid Macrocellular Living Foams. *J. Mater. Chem. B* **2016**, *4*, 2290–2303.
(35) Heim, S.; Lleo, M.; Bonato, B.; Guzman, C. A.; Canepari, P. The Viable but Nonculturable State and Starvation Are Different Stress Responses of Enterococcus Faecalis, as Determined by Proteome Analysis. *J. Bacteriol.* **2002**, *184*, 6739–6745.
(36) Johnson, P. E.; Muttil, P.; MacKenzie, D.; Carnes, E. C.; Pelowitz, J.; Mara, N. A.; Mook, W. M.; Jett, S. D.; Dunphy, D. R.; Timmins, G. S. Spray-Dried Multiscale Nano-Biocomposites Containing Living Cells. *ACS Nano* **2015**, *9*, 6961–6977.
(37) Back, J. P.; Kroll, R. G. The Differential Fluorescence of Bacteria Stained with Acridine Orange and the Effects of Heat. *J. Appl. Bacteriol.* **1991**, *71*, 51–58.
(38) Davey, H. M.; Hexley, P. Red but Not Dead? Membranes of Stressed Saccharomyces Cerevisiae Are Permeable to Propidium Iodide. *Environ. Microbiol.* **2011**, *13*, 163–171.
(39) Savage, T. J.; Dunphy, D. R.; Harbaugh, S.; Kelley-Loughnane, N.; Harper, J. C.; Brinker, C. J. Influence of Silica Matrix Composition and Functional Component Additives on the Bioactivity and Viability of Encapsulated Living Cells. *ACS Biomater. Sci. Eng.* **2015**, *1*, 1231–1238.
(40) Baca, H. K.; Ashley, C.; Carnes, E.; Lopez, D.; Flemming, J.; Dunphy, D.; Singh, S.; Chen, Z.; Liu, N.; Fan, H.; Lopez, G. P.; Brozik, S. M.; Werner-Washbume, M.; Brinker, C. J. Cell-Directed Assembly of Lipid-Silica Nanostructures Providing Extended Cell Viability. *Science* **2006**, *313*, 337–341.
(41) Lu, Y.; Fan, H.; Stump, A.; Ward, T. L.; Rieker, T.; Brinker, C. J. Aerosol-Assisted Self-Assembly of Mesostructured Spherical Nanoparticles. *Nature* **1999**, *398*, 223–226.
(42) Brinker, C. J.; Scherer, G. W. *Sol–Gel Science; The Physics and Chemistry of Sol–Gel Processing*; Academic Press: Boston, MA, 1990
(43) Wong, Y. L.; Sampson, S.; Germishuizen, W. A.; Goonesekera, S.; Caponetti, G.; Sadoff, J.; Bloom, B. R.; Edwards, D. Drying a Tuberculosis Vaccine without Freezing. *Proc. Natl. Acad. Sci. U. S. A.* **2007**, *104*, 2591–2595.
(44) Bhatia, R. B.; Brinker, C. J.; Gupta, A. K.; Singh, A. K. Aqueous Sol-Gel Process for Protein Encapsulation. *Chem. Mater.* **2000**, *12*, 2434–2441.
(45) Brinker, C. J.; Keefer, K. D.; Schaefer, D. W.; Ashley, C. S. Sol-Gel Transition in Simple Silicates. *J. Non-Cryst. Solids* **1982**, *48*, 47–64.
(46) Brinker, C. J.; Keefer, K. D.; Schaefer, D. W.; Assink, R. A.; Kay, B. D.; Ashley, C. S. Sol-Gel Transition in Simple Silicates II. *J. Non-Cryst. Solids* **1984**, *63*, 45–59.
(47) Gray, J. V.; Petsko, G. A.; Johnston, G. C.; Ringe, D.; Singer, R. A.; Werner-Washburne, M. Sleeping Beauty": Quiescence in Saccharomyces Cerevisiae. *Microbiol. Mol. Biol. Rev.* **2004**, *68*, 187–206.
(48) Ashburner, M.; Ball, C. A.; Blake, J. A.; Botstein, D.; Butler, H.; Cherry, J. M.; Davis, A. P.; Dolinski, K.; Dwight, S. S.; Eppig, J. T.; et al. Gene Ontology: Tool for the Unification of Biology. *Nat. Genet.* **2000**, *25*, 25–29.
(49) Benjamini, Y.; Hochberg, Y. Controlling the False Discovery Rate: A Practical and Powerful Approach to Multiple Testing. *J. R. Stat. Soc. B* **1995**, 289–300.
(50) Huang, D. W.; Sherman, B. T.; Lempicki, R. A. Systematic and Integrative Analysis of Large Gene Lists Using DAVID Bioinformatics Resources. *Nat. Protoc.* **2008**, *4*, 44–57.
(51) Supek, F.; Bošnjak, M.; Škunca, N.; Šmuc, T. REVIGO Summarizes and Visualizes Long Lists of Gene Ontology Terms. *PLoS One* **2011**, *6*, e21800.
(52) Boorsma, A.; de Nobel, H.; ter Riet, B.; Bargmann, B.; Brul, S.; Hellingwerf, K. J.; Klis, F. M. Characterization of the Transcriptional Response to Cell Wall Stress in Saccharomyces Cerevisiae. *Yeast* **2004**, *21*, 413–427.
(53) Neiman, A. M. Sporulation in the Budding Yeast Saccharomyces Cerevisiae. *Genetics* **2011**, *189*, 737–765.
(54) Liu, L.; Sakakibara, K.; Chen, Q.; Okamoto, K. Receptor-Mediated Mitophagy in Yeast and Mammalian Systems. *Cell Res.* **2014**, *24*, 787–795.
(55) Manjithaya, R.; Nazarko, T. Y.; Farré, J. C.; Subramani Suresh, S. Molecular Mechanism and Physiological Role of Pexophagy. *FEBS Lett.* **2010**, *584*, 1367–1373.
(56) Levin, D. E. Regulation of Cell Wall Biogenesis in Saccharomyces Cerevisiae: The Cell Wall Integrity Signaling Pathway. *Genetics* **2011**, *189*, 1145–1175.
(57) Fuchs, B. B.; Mylonakis, E. Our Paths Might Cross: The Role of the Fungal Cell Wall Integrity Pathway in Stress Response and Cross Talk with Other Stress Response Pathways. *Eukaryotic Cell* **2009**, *8*, 1616–1625.

DOI: 10.1021/acsnano.6b06385
ACS Nano 2017, 11, 3560–3575

(58) Poirier, Y.; Antonenkov, V. D.; Glumoff, T.; Hiltunen, J. K. Peroxisomal β-Oxidation—a Metabolic Pathway with Multiple Functions. *Biochim. Biophys. Acta, Mol. Cell Res.* **2006**, *1763*, 1413−1426.
(59) Swinnen, S.; Klein, M.; Carrillo, M.; McInnes, J.; Nguyen, H. T. T.; Nevoigt, E. Re-Evaluation of Glycerol Utilization in Saccharomyces Cerevisiae: Characterization of an Isolate That Grows on Glycerol without Supporting Supplements. *Biotechnol. Biofuels* **2013**, *6*, 157.
(60) Klosinska, M. M.; Crutchfield, C. A.; Bradley, P. H.; Rabinowitz, J. D.; Broach, J. R. Yeast Cells Can Access Distinct Quiescent States. *Genes Dev.* **2011**, *25*, 336−349.
(61) LaFleur, M. D.; Kumamoto, C. A.; Lewis, K. Candida Albicans Biofilms Produce Antifungal-Tolerant Persister Cells. *Antimicrob. Agents Chemother.* **2006**, *50*, 3839−3846.
(62) Lewis, K. Persister Cells, Dormancy and Infectious Disease. *Nat. Rev. Microbiol.* **2007**, *5*, 48−56.
(63) Bojsen, R.; Regenberg, B.; Gresham, D.; Folkesson, A. A Common Mechanism Involving the TORC1 Pathway Can Lead to Amphotericin B-Persistence in Biofilm and Planktonic Saccharomyces Cerevisiae Populations. *Sci. Rep.* **2016**, *6*, 21874.
(64) Bojsen, R.; Regenberg, B.; Folkesson, A. Persistence and Drug Tolerance in Pathogenic Yeast. *Curr. Genet.* **2017**, *63*, 19.
(65) Phillips, E.; Penate-Medina, O.; Zanzonico, P. B.; Carvajal, R. D.; Mohan, P.; Ye, Y.; Humm, J.; Gönen, M.; Kalaigian, H.; Schöder, H.; Strauss, H. W.; Larson, S. M.; Wiesner, U.; Bradbury, M. S. Clinical Translation of an Ultrasmall Inorganic Optical-PET Imaging Nanoparticle Probe. *Sci. Transl. Med.* **2014**, *6*, 260ra149.
(66) Wright, R. Transmission Electron Microscopy of Yeast. *Microsc. Res. Tech.* **2000**, *51*, 496−510.
(67) Smyth, G. K. *Limma: Linear Models for Microarray Data. In; Bioinformatics and computational biology solutions using R and Bioconductor*; Springer: New York, 2005; pp 397−420.
(68) Wu, Z.; Irizarry, R. A.; Gentleman, R.; Martinez-Murillo, F.; Spencer, F. A Model-Based Background Adjustment for Oligonucleotide Expression Arrays. *J. Am. Stat. Assoc.* **2004**, *99*, 909−917.
(69) *Cluster 3.0 Manual*; Stanford University: Stanford, CA, 2008.
(70) Saldanha, A. J. Java Treeview–Extensible Visualization of Microarray Data. *Bioinformatics* **2004**, *20*, 3246−3248.
(71) Kanehisa, M.; Goto, S. KEGG: Kyoto Encyclopedia of Genes and Genomes. *Nucleic Acids Res.* **2000**, *28*, 27−30.

DOI: 10.1021/acsnano.6b06385
ACS Nano 2017, 11, 3560−3575